From Microstructure to Mechanics: A Multi-constituent Micro-scale Computational Model of Arterial Tissue

M. Pétré [1,2,3], H. Wolfs [3], L. Maes [3], G. Kerckhofs [1,2,4,5] & N. Famaey [3,6]

1. Institute of Mechanics, Materials and Civil Engineering (iMMC), UCLouvain, Belgium; 2. Institut de recherche expérimentale et clinique (IREC), UCLouvain, Belgium; 3. Dpt. Mechanical Engineering, KU Leuven, Belgium; 4. Dpt. Materials Engineering, KU Leuven, Belgium; 5. Prometheus, Division of Skeletal Tissue Engineering, KU Leuven, Belgium.; 6. FIBEr, KU Leuven Core Facility for Biomechanical Experimentation

Abstract

Arterial tissues exhibit complex growth and remodeling processes, where cells continuously regulate extracellular matrix (ECM) components in response to mechanical and biochemical stimuli. Understanding the interplay between the arterial microstructure and mechanical behavior is crucial for characterizing cardiovascular diseases, such as hypertension and atherosclerosis. In this study, we developed a microstructure-based representative volume element (RVE) model of the porcine aortic medial layer, incorporating elastic lamellae, elastin fibers, collagen fibers, and smooth muscle cells. The RVE geometry was constructed using multiple imaging modalities, including contrast-enhanced X-ray microfocus computed tomography (CECT), multiphoton microscopy, classical 2D histology, and scanning electron microscopy (SEM). The mechanical properties of the RVE components were assigned based on literature data, and the model was validated against experimental tensile test data. A size convergence study determined that an RVE containing eleven medial lamellar units is necessary to obtain a representative macroscopic mechanical response. Furthermore, we analyzed mesh convergence and performed a parameter sensitivity analysis to assess the influence of mechanical and microstructural properties on the macroscopic behavior. Our results indicate that the material stiffness and volume percentages of elastin and collagen play a dominant role in the stress response. Using a homogenization approach, we quantified the contribution of each microstructural component within the representative volume element (RVE). The analysis showed that elastic lamellae dominate the initial linear region of the stress-strain curve, while the non-linear behavior is primarily governed by collagen fibers. Additionally, we analyzed the stretch distribution within the collagen network and found that stretch varies considerably across individual fibers, with the average fiber stretch remaining well below the macroscopic stretch of the RVE. Moreover, the mechanical stretch experienced by smooth muscle cells through their integrin complexes was characterized, revealing the presence of both compressive and tensile stretches. This information is highly valuable for advancing our understanding of the interactions between extracellular matrix components and how these interactions contribute to tissue remodeling in disease conditions.

Keywords: arterial tissue, microstructural imaging, representative volume element, multi-scale modeling

1. Introduction

Arterial tissues, like many biological tissues, are characterized by growth and remodeling processes, where cells continuously regulate the production and degradation of components of the extracellular matrix (ECM), both during natural aging and in response to injury or disease [1]. Homeostasis refers to the process by which cells maintain tissue functionality and structural integrity by sensing the biochemical and mechanical environment [2]. This means that not only does the microstructure influence mechanical properties, but the

mechanical environment also directly affects the microstructure of arterial tissues, a phenomenon known as mechanoregulation. This intricate relationship between arterial microstructure and mechanical behavior is also reflected in various cardiovascular diseases, such as hypertension, where increased blood pressure leads to stiffer arteries, characterized by increased collagen content and accelerated degradation of elastic lamellae [3, 4, 5]. Also in atherosclerosis, hemodynamic forces, such as perturbed flow and wall shear stress patterns, strongly correlate with atherosclerotic plaque development in addition to systemic risk factors (e.g. smoking, obesity...) [6, 7].

In the past, much focus has been put on the development of constitutive phenomenological models, where the macroscopic behavior of the tissue is described by a set of equations with only an indirect link to the microstructural components. A large number of such constitutive models exist [2, 8, 9, 10], the most well-known being the Gasser-Ogden-Holzapfel (GOH) model, where the mechanical behavior of arterial tissue can be described using a transversely isotropic strain energy density function with five material parameters [11]. Although this class of constitutive models is computationally efficient for numerical simulation at the tissue scale, they often lack the ability to capture the underlying microstructural mechanisms that govern the tissue's adaptive response, such as cellular activity and ECM remodeling. Therefore, more fine-grained models are needed to better understand the underlying mechanotransduction processes. To maintain computational efficiency even at this level, multiscale modeling techniques can be used, e.g. based on representative volume elements (RVEs) [12, 13].

RVE modeling provides a discrete representation of microstructural components in a representative volume of the material. This allows the quantitative analysis of individual component deformation and loading, as well as of the interactions between the components, which are essential metrics to understand ECM degradation. When also cells are modelled, mechanical loading of these cells can be linked to ECM production, e.g. through gene regulatory networks [14]. By applying appropriate boundary conditions and homogenization techniques to the RVE [12, 15, 16], the microscale mechanics can then be linked back to the macroscale mechanical behaviour. When properly validated, such RVE models can be used to test hypotheses regarding certain arterial pathologies associated with ECM remodeling, by relating the simulations to clinically observed changes in the overall mechanical behavior of the artery, and/or to tissue-scale mechanical tests.
Several studies have already investigated the potential of multiscale RVE modeling for arterial tissue [17, 18, 19, 20, 21, 22]. A comprehensive review is provided by Dalbosco et al. [23] and the most relevant studies are briefly discussed below. Thunes et al. investigated the dissection mechanism in ascending aortic tissue based on cohorts of non-aneurysmal and aneurysmal patients [17]. They developed an RVE based on a single lamellar unit (LU), including two elastic lamellae, resulting in a volume fraction of 12%. The interlamellar space (68%) was modeled with a planar network of collagen fibers represented by straight truss elements with a fiber diameter of 3 μm. The crimp of collagen fibers was not explicitly represented in the model but was taken into account through the use of the recruitment stretch concept in the constitutive model [22, 24]. In addition to recruitment stretch, fiber damage was also included in the model, occurring when a critical stretch value is reached. However, their model did not account for the typical out-of-plane distribution characteristics of collagen fibers in arterial tissue. Moreover, the elastic lamellar thickness they considered was extremely small compared to values reported in the literature [25, 26]. Additionally, they did not investigate the effect of RVE size on the homogenized mechanical behavior considering only a single LU.
Following a similar approach, Mahutga and Barocas developed a LU-based RVE to study the pathophysiological aspects of aortic growth, remodeling, and failure in cases of hypertension and aneurysm [18]. Their model incorporated growth and remodeling laws applied directly to individual discrete fibers. They modeled one elastic lamella as a 2D network of trusses composed of collagen and elastin, combined with a 3D network of trusses representing actin filaments, corresponding to smooth muscle cells. Their RVE model represents only a single LU with physical dimensions of [20 μm x 20 μm x 10 μm], which may not fully capture the characteristics of the media layer due to its limited size. Indeed, a porcine medial aorta typically consists of 70 elastic lamellae and is on average 1400 μm thick [25]. Furthermore, the elastic lamella in their model were treated as a planar network of elastin and collagen fibers. However, in reality, elastic lamellae

are thick sheets of elastin separated by an interlamellar space filled with collagen and smooth muscle cells [27]. Moreover, the characteristic out-of-plane angle distribution of collagen fibers was neglected, as they modeled it as a 2D network.

To tackle the limitations related to the characteristic out-of-plane distribution of collagen fibers, Dalbosco et al. developed an RVE model consisting of a 3D ground matrix reinforced with 1D collagen fibers [22]. Two collagen fiber families were considered, characterized by two in-plane angle distributions with opposite mean fiber angles, as well as an out-of-plane distribution. Multiple RVE sizes as well as different boundary conditions were investigated, and size convergence was achieved for an RVE of dimensions [120 μm x 120 μm x 60 μm], when applying periodic boundary conditions. Moreover, among the four different boundary conditions tested, periodic boundary conditions proved to be the most effective for model convergence and for minimizing dependencies on the RVE size. However, the model only accounted for the ground substance and collagen fibers, such that interactions between these components and the elastin or smooth muscle cells could not be studied.

Addressing the current limitations, this work aims to develop a more microstructurally accurate RVE model for the aortic medial layer. The approach extends the formulation of Dalbosco et al. for collagen fibers and incorporates elastin and smooth muscle cells into the framework. Focusing on the medial layer of healthy porcine aorta, the RVE model is constructed based on microstructural information derived from several imaging modalities, including contrast-enhanced X-ray microfocus computed tomography (CECT), multiphoton microscopy, classical 2D histology, and scanning electron microscopy (SEM). Designed to be fully parameterized, the model allows for quick and efficient modifications of the microstructure. The influence of the RVE size on the homogenized mechanical behavior has been investigated, along with a parameter sensitivity study. The RVE model was then validated against experimental uniaxial tensile tests in both the circumferential and axial directions. Finally, the impact of microstructural changes in the RVE model was investigated, as well as the role each RVE component plays in the macroscopic stress response.

2. Methods

2.1. Building the RVE geometry

2.1.1. Elastin

The aortic wall consists of three distinct layers: the intima, media, and adventitia. Among these, the media is the thickest layer, particularly in elastic arteries such as the aorta [25]. This media layer is organized into medial lamellar units (MLUs), which serves as the fundamental structural and functional components of the aortic wall [27]. A MLU is composed of thick and continuous elastin lamellar sheets, also called elastic lamellae. Thanks to CECT, the elastic lamellae in healthy porcine aorta can be visualised and structurally quantified in 3D (Fig. 1.a). According to Leyssens et al., the thickness of the elastic lamellae average to 15 μm, with the interlamellar space also having an average thickness of 15 μm [25]. The elastic lamellae constitute, on average, 60% of the medial layer's volume fraction. Sherifova et al., assessed the microstructural organisation of human thoracic aorta using classical 2D histology and second harmonic generation (SHG) [26]. They also state that elastic lamellae have a typical thickness of 13-15 μm and a volume fraction ranging from 25% to 50%.

The interlamellar space is filled with elastin, collagen and smooth muscle cells. According to O'Connell et al., the elastin within the interlamellar space can be separated into thin interlamellar elastin fibers (IEFs) and thick radial struts (90% of the lamellar thickness), which serve to connect one elastic lamella to the next, as shown in Figure 1.b [27]. Unfortunately, the resolution of CECT imaging did not yet allow one to visualize components found in the interlamellar space [25]. However, it was observed that the elastic lamellae exhibit a certain degree of tortuosity and are interconnected through the merging of adjacent elastic sheets rather than by radial struts [25]. In contrast, scanning electron microscopy has enabled O'Connell et al. to analyze the medial layer of a rat aorta [27]. They showed that medial elastin is composed of 71% the

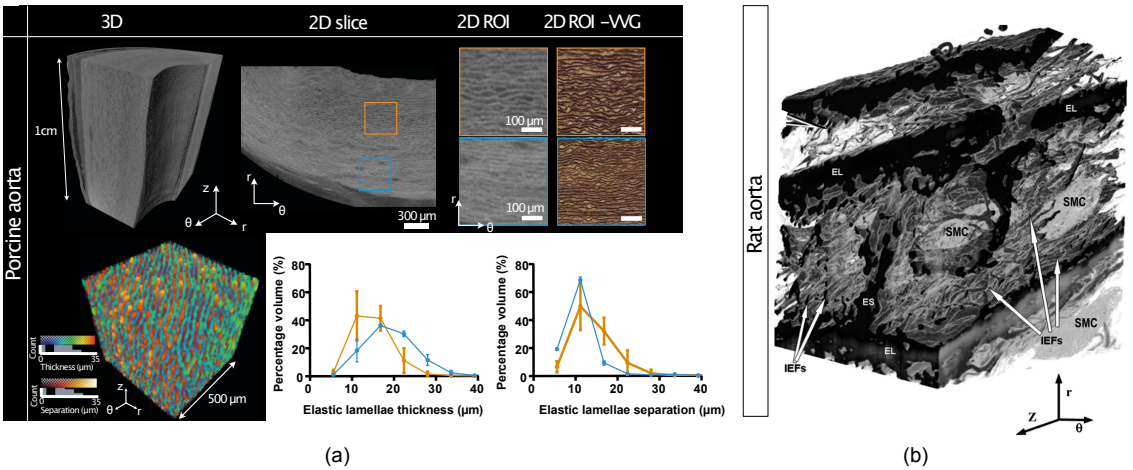


Fig. 1: (a) Contrast-enhanced microCT image of a porcine aorta, where the elastic lamellae are visible in light grey. A 3D representation of a 1cm × 1cm sample is shown, along with the corresponding 2D slice. Two regions of interest (ROIs) in the media layer are highlighted: one closer to the intima, in orange, and another closer to the adventitial layer in blue. These ROIs are compared with classical 2D histology using Verhoeff's Van Gieson stain (VVG). The thickness and spacing of the elastic lamellae in both regions are characterized in 3D, and a 3D representation is shown with lamellae thickness represented in green and spacing in orange (adapted from and with kind permission from [25], licensed under the Creative Commons Attribution 4.0 International License [28]). (b) Serial block-face scanning electron microscopy image of rat aorta shows the medial lamellar unit. Thick elastic lamellae form a sandwich structure where smooth muscle cells, interlamellar elastic fibers and elastin struts reside. Volume size of [22μm x 16μm × 25μm] (adapted from and with kind permission from [27], licensed under the Creative Commons Attribution 4.0 International License [28]).

elastic lamellae, 27% IEFs and 2% radial thick struts.

In this work, we hypothesized that the percentages given by O'Connell are also representative of the porcine aorta and we have adapted them slightly for simplicity and symmetry within the RVE framework (Table 1). In our RVE model, elastic lamellae account for 50%, the interlammelar elastin fibers 5%, and the elastin struts 1%. Because the merging of two elastic sheets is challenging to represent geometrically, radial struts were introduced in the model to approximate these interconnections. The lamella thickness and the interlamellar spacing were 15 μm. Moreover, the elastic lamellae are aligned in the circumferential direction, while the IEFs and elastin struts exhibit a tilt angle of approximately 20° relative to the circumferential direction as stated by [27, 29, 30]. Table 1 provides a summary of the reported values, along with the parameters selected for building our RVE model.

2.1.2. Smooth muscle cells

Smooth muscle cells (SMC) are present in the interlamellar space and exhibit a fusiform shape with elliptical cell nuclei. The long axis has been reported to be $19 \pm 3.3 \mu m$ and the short axis $3.1 \pm 0.8 \mu m$ [27]. The SMCs have been described to be oriented at an angle of 19° relative to the circumferential direction [27, 29, 30]. The volume fraction of SMCs in the rat aorta was determined as approximately 24% [27] and ranging from 10% to 50% in the human aorta [26, 31] (Table 1).

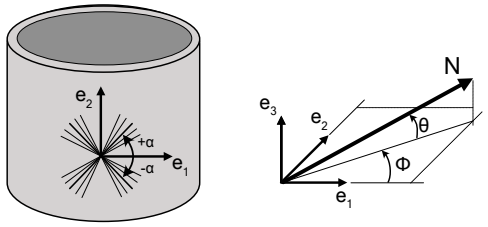
2.1.3. Collagen fibers

Recently, Niestrawska et al. quantified the diameter of collagen fibers in the medial and adventitial layers, separately, of healthy human abdominal aortas using second-harmonic generation (SHG) [32]. They found that the collagen fibers in the medial layer were 3 μm [2.6-3.6 μm] , whereas those in the adventitia were much thicker 21.9 μm [20.2-23.9 μm].

Table 1: Microstructural parameters for all RVE components as reported in the literature (i.e. experimental value) and implemented into our RVE framework (i.e. simulated value). Orientation are given with respect to the circumferential direction.

Elastic lamellae			
Parameter	**Experimental value**	**Simulated value**	**References**
Volume Fraction V_{el}	[25% - 60%]	50%	[25, 26]
Orientation	0°	0°	[25, 27]
Thickness	[13 - 15] μm	15 μm	[25, 26]
Interlamellar space	[7 - 20] μm	15 μm	[25]
Interlamellar elastin fibers			
Parameter	**Experimental value**	**Simulated value**	**References**
Volume fraction V_{IEF}	[6.75% - 16.2%]	5%	[27]
Orientation	20°	20°	[27]
Diameter d_{ief}	[11.7 - 13.5] μm	13.5 μm	[27]
Elastin struts			
Parameter	**Experimental value**	**Simulated value**	**References**
Volume fraction V_{es}	[0.5% - 1.2%]	1%	[27]
Orientation	20°	20°	[27]
Diameter d_{ief}	[1.3 - 1.5] μm	1.5 μm	[27]
Smooth muscle cells			
Parameter	**Experimental value**	**Simulated value**	**References**
Shape	Fusiform	Ellipsoid	[27, 20]
Dimensions	[19 ± 3.3; 3.1 ± 0.8] μm	[19, 3, 3] μm	[27]
Volume fraction V_f	[10% - 50%]	14%	[27, 29, 30]
Orientation	[19.1 ± 2.8 °]	19°	[27]
Collagen fibers			
Parameter	**Experimental value**	**Simulated value**	**References**
Diameter d	[2.6 μm - 3.6 μm]	3 μm	[22, 32]
Mean reference length L_f	120 μm	120 μm	[33]
Volume fraction V_f	[10% - 40%]	30%	[26, 34]
In-plane fiber angle α	[6.91° - 21°]	6.91°	[35, 32]
Out-of-plane fiber angle	0°	0°	[32, 36, 35]
In-plane fiber dispersion κ_{ip}	[0.18 - 0.41]	0.28	[22, 26, 32, 37]
Out-of-plane fiber dispersion κ_{op}	[0.41 - 0.5]	0.493	[22, 26, 32]

The collagen fiber content was reported to vary from 20% to 40% in the medial layer of the human thoracic descending aorta [26] and from 10% to 30% in the medial layer of the porcine thoracic descending aorta [34]. Niestrawska et al. found that collagen fibers are aligned along two preferred directions within the circumferential-axial plane of arterial tissue, exhibiting some degree of dispersion. These fiber orientations can be characterized by $\pm\alpha$ angles with respect to the circumferential axis, which vary depending on the type of artery and the specific layer analyzed (Fig. 2.a). In the axial-radial plane, collagen fibers have been described to be nearly parallel to the axial axis, exhibiting lower degree of dispersion than in the circumferential-axial plane.



(a) (b)

Fig. 2: Schematic representation of the collagen fiber orientation. (a) Two symmetric fiber families in the circumferential-axial plane and (b) fiber N described in terms of azimuthal (also known as in-plane angle), (Φ) and elevation (also known as out-of-plane angle), (θ).

In order to characterize the 3D fiber orientation in our RVE model, consider coordinate system (e_1, e_2, e_3), which represents the circumferential, axial and radial direction, respectively. N, the fiber vector, can be defined by two angles: the azimuthal Φ or the in-plane angle and the elevation angle Θ, also called the out-of-plane angle, such that

$$N(\Phi, \Theta) = cos(\Phi)cos(\Theta)e_1 + sin(\Phi)cos(\Theta)e_2 + sin(\Theta)e_3 \tag{1}$$

where $\Phi \in [0, 2\pi]$ and $\Theta \in [-\pi/2, +\pi/2]$.

To describe the dispersion of the fiber angles, we used bivariate von Mises distributions similarly as in Dalbosco et al. [22], where independent probability distributions for each fiber angle are assumed:

$$\rho(\Phi, \Theta) = \rho_{ip}(\Phi)\rho_{op}(\Theta) \tag{2}$$

$\rho_{ip}(\Phi)$ and $\rho_{op}(\Theta)$ can be defined as:

$$\rho_{ip}(\Phi) = \frac{exp[a\ cos(2[\Phi \pm \alpha])]}{I_0(a)} \tag{3}$$

$$\rho_{op}(\Theta) = 2\sqrt{\frac{2b}{\pi}}\frac{exp[b(cos(2\theta) - 1)]}{erf(\sqrt{2b})} \tag{4}$$

where a and b are concentration parameters, α the mean fiber in-plane angle, I_0 the modified Bessel function of first kind of order zero and erf the error function. The mean fiber out-of-plane angle is assumed to be zero, as described in [22, 36]. The mean in-plane angle varies from 6° to 51° in the healthy human descending thoracic aorta, as obtained via second harmonic generation, with a mean around 15° reported by Sherifova et al. [26]. Niestrawska et al. reported a mean in-plane fiber angle of 6.91° in healthy human abdominal aortas, using second harmonic generation, in a 2016 study [35]. In a subsequent study published in 2022, they reported a slightly higher mean angle of 10° [7°-21°] for the same tissue type [32].

With this information, it is possible to link the concentration parameters a and b with scalar quantities describing the in-plane and out-of-plane dispersion [36, 35], as:

$$\kappa_{ip} = \frac{1}{2} - \frac{I_1(a)}{2I_0(a)} \qquad and \qquad \kappa_{op} = \frac{1}{2} - \frac{1}{8b} + \frac{1}{4}\sqrt{\frac{2}{\pi b}}\frac{exp(-2b)}{erf(\sqrt{2b})} \tag{5}$$

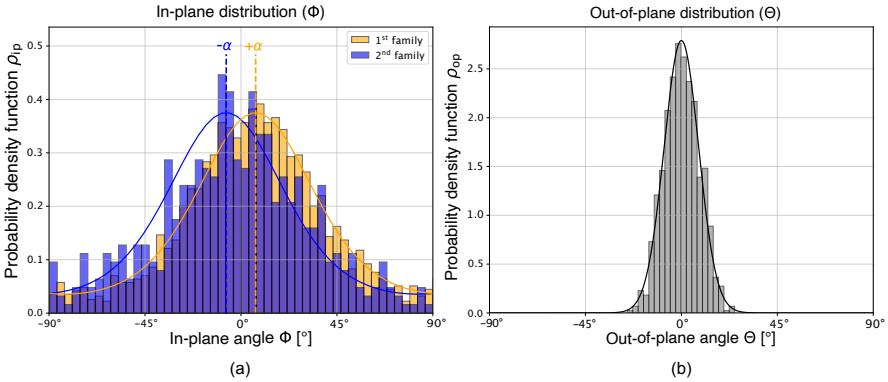


Fig. 3: (a) In-plane fiber angle distributions with a mean angle of $\alpha = \pm 6.91°$. (b) The out-of-plane fiber angle distribution for a mean angle of 0°.

2.1.4. *Generation of the RVE medial lamellar unit*

The RVE model replicates the medial lamellar unit found in elastic arteries, specifically in the porcine thoracic descending aorta. A Python script was developed to automatically and fully parametrically generate the geometry of all components described above using the PyVista toolbox [38]. The script creates geometrical objects that are then meshed and exported as input files for finite element analysis (FEA) in the Abaqus software (Dassault Systèmes) using a classic implicit FE solver. It begins by defining the size of the RVE and constructing it as a solid cube representing the ground matrix into which all other components are embedded. 8-node linear hexahedron hybrid elements (C3D8H) were used to mesh the ground matrix. The elastic lamellae were represented as rectangular parallelepipeds , evenly spaced by interlamellar spaces (Fig. 4).

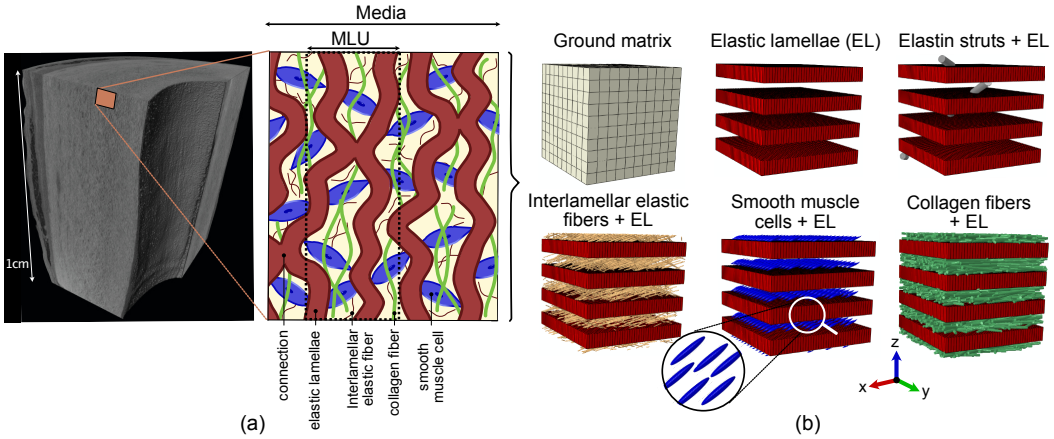


Fig. 4: (a) A 3D CECT image of a porcine aorta (adapted from [25]), with a simplified schematic of the medial lamellar unit complex based on the CECT data. (b) The RVE model showing: elastic lamellae (red), elastin struts (gray), interlamellar elastic fibers (orange), smooth muscle cells (blue), and collagen fibers (green) within a (beige) ground matrix. The RVE, with a cubic size of $120^3 \mu m^3$, is selected for visualization purposes and does not correspond to the converged size (see Section 3.1).

Quadratic shell elements (S4R) were selected for the elastic lamellae. The elastin struts serve as connection between the elastic lamellae and, for simplicity, were represented by linear truss elements (T3D2). Similarly, interlamellar elastic fibers and collagen fibers were added between the elastic lamellae, aligned with their preferred orientation and also represented by linear truss elements (T3D2) (Fig. 4.b). The T3D2 element is a two-node linear truss element used in 3D to model slender, line-like structures that support only axial loading along the element, meaning that it can carry tension and compression, but not bending, shear, or torsion. Smooth muscle cells were then added and represented as ellipsoids meshed with 10-node quadratic tetrahedron hybrid elements (C3D10H). Periodicity was applied to the RVE model by including only half of the interlamellar space at the top and bottom, enabling seamless stacking of the RVE models (Fig. 5.a). Moreover, periodicity is applied to all fibers. This means that if a fiber exits the RVE domain before reaching its full length L_f, it re-enters symmetrically on the opposite side of the cube, with the remaining length continuing as illustrated by the blue fiber in Figure 5.b. If the fiber stays within the boundaries, no symmetry is applied, as depicted by the orange fiber (Fig. 5.b). This ensures faster convergence in the FEA. More details on how the geometry of the RVE model was generated can be found in Appendix A.

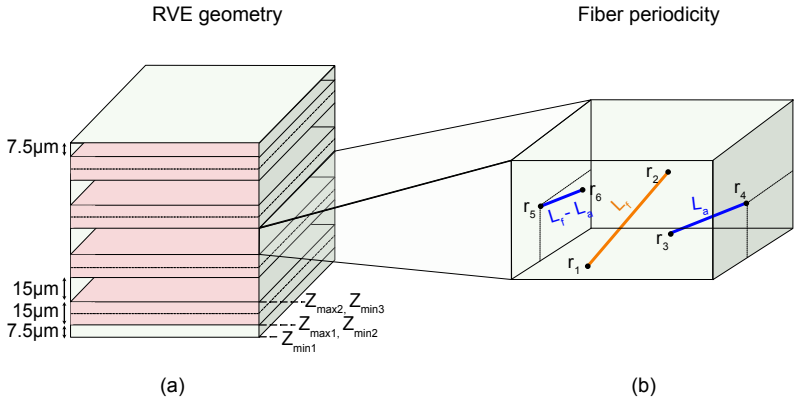


Fig. 5: (a) Schematic overview of an RVE ($120^3 \mu m^3$ in size) with 50% elastic lamellae, defining the elastic lamellae and the inter-lamellar regions, where fibers and smooth muscle cells will be added along the respective z-boundaries (more details in Appendix A). (b) Schematic representation of the periodicity applied to the fibers in the RVE model. If a fiber exits the RVE domain before reaching its full length L_f, it re-enters symmetrically on the opposite side of the cube, continuing with the remaining length and keeping the same fiber orientation as illustrated by the blue fiber.

2.2. *Material properties*

Following a similar approach as in Dalbosco et al. [22], we selected a hyperelastic neo-Hookean material model for the ground matrix, as well as for all the elastin components and SMCs. The generic strain energy density function can be expressed as:

$$\Psi(\overline{\mathbf{C}}) = C_{10}(\bar{I}_1 - 3) + \frac{1}{D_1}(J-1)^2 \tag{6}$$

where $J = \det(\mathbf{F})$, with $\mathbf{F}$ being the deformation gradient defined as $\mathbf{F} = \frac{\partial x}{\partial X}$.
The first invariant of $\overline{\mathbf{C}}$, the deviatoric right Cauchy-Green strain tensor, is written as:

$$I_1 = \text{trace}(\overline{\mathbf{C}}) = \mathbf{I} : \overline{\mathbf{C}} \tag{7}$$

where $\overline{\mathbf{C}} = \overline{\mathbf{F}} \cdot \overline{\mathbf{F}}^T$ and $\overline{\mathbf{F}} = J^{-2/3}\mathbf{F}$.

For each structural component, different material parameters, C_{10} and D_1, were used. The parameter $C_{10} = \frac{\mu}{2}$, where μ represents the shear modulus. The parameter D_1 is a volumetric penalty parameter, chosen such that the Poisson ratio $\nu = 0.495$. Table 2 indicates the different values selected for the ground matrix, elastin

and SMCs in the RVE model and their references. The same elastin material properties were applied to the elastic lamellae, interlamellar elastin fibers and elastin struts.

Table 2: Neo-Hookean material parameters C_{10} and D_1 selected in the RVE framework for the ground matrix, elastin components and smooth muscle cells.

Structural component	**Reported value** C_{10}	**Simulated value** C_{10}	**Simulated value** D_1	**References**
Ground matrix	[0.1 kPa - 8.04 kPa]	8.04 [kPa]	3.69 10^{-3} $\left[\frac{1}{kPa}\right]$	[20, 22, 35]
Elastin	[0.1 MPa - 1.1 MPa]	0.1 [MPa]	0.297 $\left[\frac{1}{MPa}\right]$	[20, 39, 40] [41, 42]
Smooth muscle cells	[3.5 kPa - 100 kPa]	28 [kPa]	1.06 10^{-3} $\left[\frac{1}{kPa}\right]$	[20, 43, 44]

Collagen fibers exhibit a characteristic waviness, requiring them to unfold before contributing to the mechanical behavior when stretched [20]. Since this waviness is not explicitly represented in our RVE model, the selected material model accounts for this unfolding process by introducing the concept of recruitment stretch [20, 22]. Accordingly, the strain energy density function in our RVE model was expressed as:

$$\Psi_{c_i}(\lambda) = \begin{cases} 0, & \text{if } 0 < \lambda < \lambda_{r_i} \\ \frac{E_f}{2}(\lambda - \lambda_{r_i})^2, & \text{if } \lambda > \lambda_{r_i} \end{cases} \tag{8}$$

where λ is the stretch in the fiber direction, λ_{r_i} is the recruitment stretch of the i^{th} fiber and E_f the fiber axial stiffness. As collagen fibers exhibit varying degrees of waviness, a distribution of recruitment stretch values was introduced, ensuring that each fiber is assigned a specific recruitment stretch. This material model was implemented as a user-defined material subroutine (UMAT) in Abaqus. Following a common approach [22, 24, 45], a beta distribution was introduced to define the recruitment stretches:

$$\rho_r(\lambda_r) = \frac{(\lambda_r - \lambda_1)^{a_1 - 1}\,(\lambda_2 - \lambda_r)^{a_2 - 1}}{\beta(a_1, a_2)\,(\lambda_2 - \lambda_1)^{a_1 + a_2 - 2}} \tag{9}$$

where a_1 and a_2 are the shape parameters, and λ_1 and λ_2 represent the bounds of the distribution—λ_1 being the minimum stretch at which fibers are recruited, and λ_2 the maximum stretch at which all fibers are recruited. The recruitment stretch of collagen fibers is rarely described in the literature, as it is primarily a mathematical concept used in computational modeling approaches. Therefore, we assumed in our RVE model that collagen is fully recruited once the supraphysiological strain is reached. Physiological axial strain is reported to range from 40% to 60% in porcine carotid arteries [46]. Additionally, Weisbecker et al. studied the recruitment stretch in human thoracic aortas by applying a computational approach and fitting the experimental data to the recruitment stretch model [45]. The constitutive parameters used for collagen in our RVE model are listed in Table 3 and Figure 6 shows the beta distribution for the recruitment stretch selected in our RVE model.

2.3. Embedded elements

The embedded elements technique is commonly applied in fiber-reinforced materials, such as reinforced composites or concrete [50, 51, 52]. It involves defining a host region that contains one or more embedded regions. In our case, the host region was the solid ground matrix, within which all other structural elements are embedded. This method enables a smoother mesh generation, as it avoids the need to cut the host material and merge it with the embedded part. The technique assumes that both the embedded and host regions are complete; they can be meshed separately and then combined in the FEA. By using embedded elements, the FE solver applies embedded constraints, such that the displacements of the embedded nodes depend on the displacements of the host nodes [53].

Table 3: Constitutive material parameters selected in the RVE framework for the collagen fibers.

Parameter	**Reported value**	**Simulated value**	**References**
Uniaxial fiber stiffness E_f	[4.7 MPa - 1.17 GPa]	54.3 [MPa]	[33, 47, 48, 49]
Shape parameters ($a_1 = a_2$)	[1.41 - 1.96]	1.90	[45]
Min. recruitment stretch value λ_1	[1 - 1.40]	1.323	[45, 46]
Max. recruitment stretch value λ_2	[1.14 - 1.60]	1.523	[45, 46]

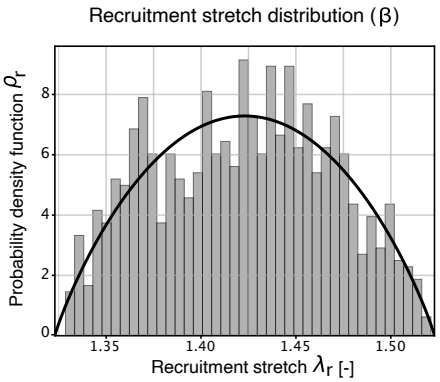


Fig. 6: Beta distribution for the recruitment stretches selected in our RVE model. The minimum recruitment stretch value, λ_1, is equal to 1.323 and the maximum recruitment stretch value, λ_2, is equal to 1.523. The black curve represents the density function ρ_r, whereas the bars are the random sampling corresponding to ρ_r

.

2.4. Boundary conditions

Periodic boundary conditions (PBC) were applied to the RVE model. This implies maintaining the same displacement differences between opposite faces of the RVE, ensuring periodicity, without enforcing the faces to remain straight (Fig. 7.a) [54]. PBC prescribe the displacement differences between corresponding nodes on opposite faces of the RVE:

$$u_i^+ - u_i^- = \overline{\epsilon}_{ij}(x_j^+ - x_j^-) \qquad on\ \delta V \tag{10}$$

where u_i is the i^{th} nodal displacement and the subscripts + and − refer to the opposite faces of the RVE, $\overline{\epsilon}_{ij}$ is the macroscopic strain and V the volume of the RVE.

To implement PBC in Abaqus, we considered a cube domain of length L (Fig.7.b), where the origin corresponds to node (0,0,0). Node sets were created for each face; however, to avoid redundancy in the constraints, front and back faces contain all nodes, whereas left and right faces contain all nodes, except for one node layer adjacent to the back face. The nodes selected are indicated by the greyed zone in Figure 7.b. The top and bottom faces contain all nodes, except for two node layers; one adjacent to the back face, and one adjacent to the right face.

Three master nodes have been defined (M_1, M_2, M_3), one for each degree of freedom, and all possess the

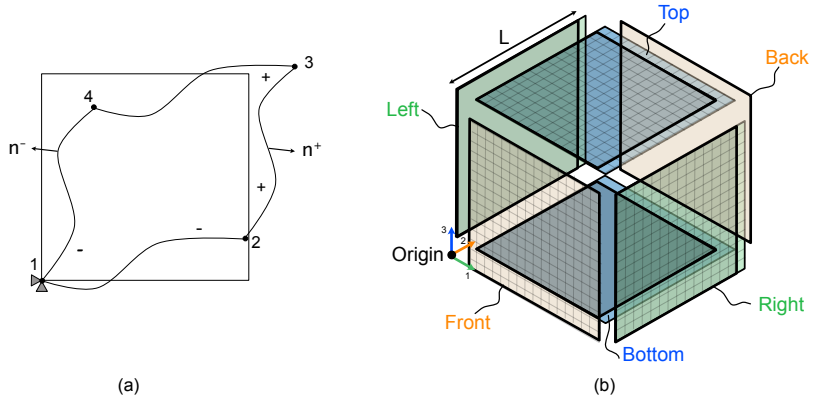


Fig. 7: (a) Periodic boundary conditions maintain the same displacement difference between opposite faces of the RVE (ensuring periodicity), but without enforcing the faces to remain straight. (b) Sketch of the RVE geometry and node sets.

origin as coordinate (an arbitrary choice). The periodic boundary conditions can be written as:

$$u_i^{(R)} - u_i^{(L)} = u_i^{(M_1)} \tag{11}$$

$$u_i^{(F)} - u_i^{(Bk)} = u_i^{(M_2)} \tag{12}$$

$$u_i^{(T)} - u_i^{(Bm)} = u_i^{(M_3)} \tag{13}$$

where u_i is the displacement of the boundary nodes belonging to either the right face (R), left face (L), front face (F), back face (Bk), top face (T), or bottom face (Bm), as well as the displacements of the master nodes.

Equations (11)-(13) set a constraint between the displacement of the boundary nodes and the displacements of the master nodes. Further details on how constraints between degrees of freedom and the displacements of the master nodes have been defined can be found in the Annex Appendix B.

2.5. Homogenization

After completing the FE analysis, the macroscopic stress was determined using two classical homogenization approaches. The first approach consisted in defining the macroscopic stress and logarithmic strain as the volume averages of the microscopic stresses and strains within the RVE.

$$\overline{\varepsilon}_{ij} = \frac{1}{V}\int_V \varepsilon_{ij}\, dV \tag{14}$$

$$\overline{\sigma}_{ij} = \frac{1}{V}\int_V \sigma_{ij}\, dV \tag{15}$$

where V is the volume of the RVE. This approach enables to obtain individual contributions from each microstructural component in the RVE model, providing a detailed understanding of their respective roles in the overall mechanical behavior.

The second approach used the traction field on the surface of interest [16, 55, 54, 56], where the macroscopic stress can be written as:

$$\int_V \sigma_{ij}\, dV = \int_{\delta V} t_j x_i\, dA \tag{16}$$

This second approach was used for all results presented below, except for section 3.4, where volumetric averaging (eq. 14) was performed to determine individual RVE components contribution. More details on the mathematical explanation of equation 16 can be found in Appendix C.

2.6. Loading scenarios

With the application of periodic boundary conditions, we precisely controlled the displacements of the master nodes, allowing to simulate various loading scenarios. We focused on two loading conditions: uniaxial tensile tests and planar biaxial tests. Uniaxial tensile tests were used to validate the RVE model against experimental data, while planar biaxial tests enabled the identification of GOH parameters across different RVE configurations, each with distinct material and microstructural properties. A parameter fitting approach was employed to identify the five material parameters of the GOH model, as described in [57, 58, 59]. The GOH strain energy density function can be written as:

$$\Psi = C_{10}(I_1 - 3) + \sum_{i=4,6} \frac{k_1}{2k_2}(\exp[k_2(I_i^* - 1)^2] - 1)) - p(J - 1) \tag{17}$$

The first term of equation 17 represents the ground matrix (excluding collagen fibers) and is modeled as an isotropic Neo-Hookean material model, where C_{10} is a stress like material parameter representing the matrix stiffness, and I_1 is the first invariant of the right Cauchy Green stretch tensor $\mathbf{C} = \mathbf{F}^T\mathbf{F}$. The second term of equation 17 represents the anisotropic contribution from the collagen fibers, with I_i pseudo-invariants of $\mathbf{C}$, representing the stretch along the preferred fiber direction. k_1, k_2 and κ represents the fiber stiffness, stiffening, and dispersion parameters, respectively. The last term of equation 17, p, is the Lagrangian multiplier introduced for incompressible materials, and J the determinant of $\mathbf{F}$.

To estimate the GOH material parameters, the GOH model forces have been compared with the RVE reaction forces obtained by performing a virtual equibiaxial tensile test. It consisted of minimizing an objective function that expresses the differences between the reaction forces predicted by the GOH model, $f_{i,j}^{mod}$, and those obtained from the RVE model, $f_{i,j}^{RVE}$ [59]:

$$\min_p \left\{ \sum_{i=1,2} \sum_{j=1}^{n} [f_{ii}^{RVE}(t_j) - f_{ii}^{mod}(F_{ii}(t_j), A, p)]^2 \right\} \tag{18}$$

where t_j represents the sampling point of the measured force and n the total amount of sampling points. $\mathbf{F}(t_j)$ is the deformation gradient at time t_j and A the cross-sectional area.

The optimization problem was solved in Python using the non-linear least square method as implemented in [57, 58, 59]. Twenty different start points were used to find a global minimum, as it was found to be an optimal number to guarantee a global minimum. Indeed, less than five starting points is not recommended, as it increases the risk of converging to a local minimum. Increasing the number beyond 20 has been shown to have minimal impact on the outcome, while increasing the computational cost.

3. Results

3.1. Model verification

To assess the influence of the RVE size on the macroscopic stress and strain response, five RVEs of increasing dimensions were constructed, with cube size of 60^3, 120^3, 240^3, 360^3 and 480^3 μm^3, respectively (Fig. 8.a). The number of elastic lamellae doubled with each doubling of size. Virtual uniaxial tensile tests with a 60% stretch were conducted on each of the five RVEs in both the circumferential and axial directions. A consistent mechanical behavior is reached for RVE 4, with cubic size 360^3 μm^3 (Fig.8.b). The root mean square error (RMSE) between RVE 4 and RVE 5 is 0.6% in the circumferential direction and 0.1% in the axial direction. In comparison, the RMSE between RVE 3 and RVE 5 was 1.6% circumferentially and 0.4% axially. Therefore, RVE 4 was selected for all subsequent analyses of this study.

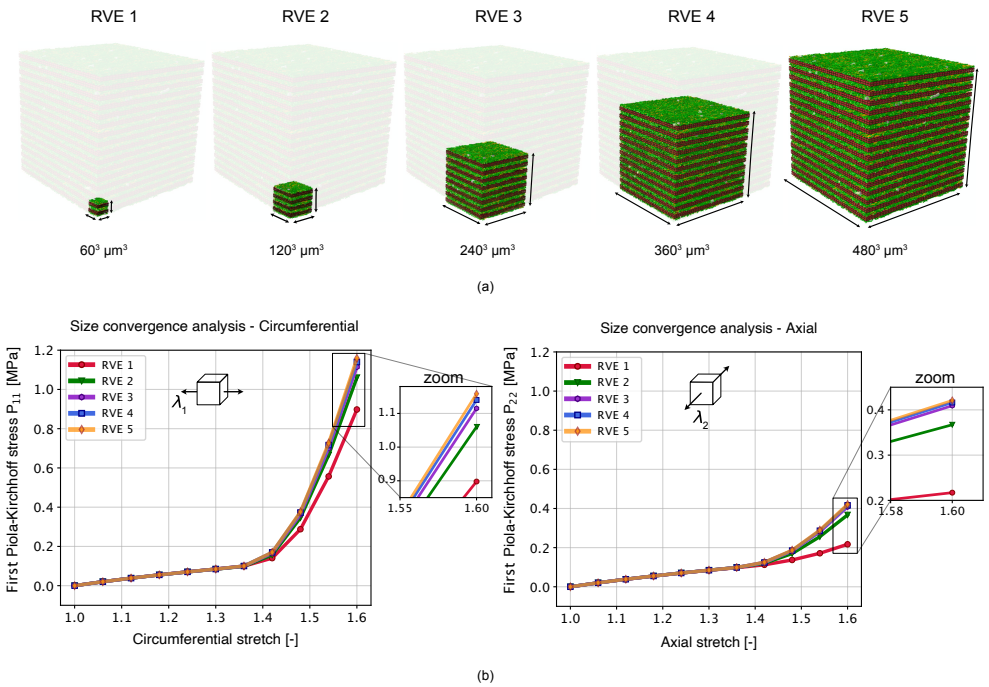


Fig. 8: (a) RVE 1 (smallest) to RVE 5 (largest) are constructed with the same microstructural parameters defined in Table 1-5. (b) Homogenized (macroscopic) stress response in the circumferential and axial directions, for the five RVE sizes. The curves obtained numerically show an overlap between RVE size 4 and size 5, with a RMSE of 0.6% circumferentially and 0.1% axially.

To investigate the mesh convergence for RVE 4, seven different mesh sizes of the ground matrix were selected with characteristic element sizes of 66, 60, 48, 42, 36, 30 and 24μm. For reference, mesh 1 corresponds to the coarsest mesh (66μm), while mesh 7 represents the finest mesh (24μm), following the order in which they appear. The mesh size of the other embedded components was kept constant. Each elastic lamella was meshed with 1600 elements, while each SMC contained 157 elements. Each fiber was divided into multiple segments based on the domain length, ensuring that each element has a length of 18 μm, which corresponds to 5% of the RVE size. Mesh convergence is achieved with mesh 7 (Fig. 9). The difference in the macroscopic First Piola-Kirchhoff stress between mesh 6 and mesh 7 was less than 0.01% at a stretch level of 30%, where collagen fibers begin to contribute, and 0.05% at a stretch level of 60%, where all collagen fibers are fully recruited. This discrepancy is likely due to the discretization of the collagen fiber mesh, which was kept constant for this analysis but may need to vary according to the host mesh size.

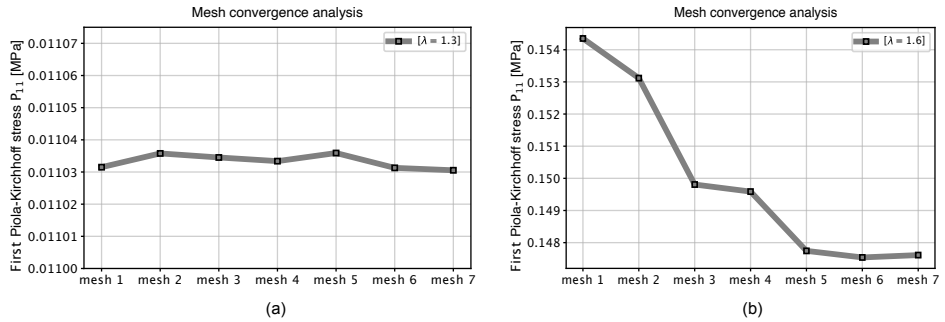


Fig. 9: Mesh convergence analysis on seven different mesh sizes. A convergence is obtained for mesh 7 (24μm). (a) The macroscopic stress at stretch of $\lambda = 1.3$ is computed for all seven meshes. (b) The macroscopic stress at stretch of $\lambda = 1.6$ is computed for all seven meshes.

3.2. Parameter sensitivity analysis

Next, a parameter sensitivity analysis was conducted on the mechanical and microstructural input parameters of our RVE model. For every parameter, a reference value and a range was retrieved from literature. The parameter was then discreetly varied from the reference value with ± 10 and 20%, whereby the percentage is calculated with respect to the reported range. In total, 11 parameters were varied one at a time, resulting in 44 simulations of biaxial tensile tests. On average, a simulation takes around 20 minutes to complete with 4 CPUs and an Intel(R) Xeon(R) Gold 6152 CPU processor with 96GB RAM. For every parameter, the tangential stiffness of the resulting circumferential stress-strain curves was evaluated at a strain of 30% (end of the toe region) and 60% (exponential part) and compared to the reference RVE represented by the black 0% line. Figure 10 illustrates variations in tangential stiffness, highlighting increases or decreases relative to the reference. Figure 11 illustrates the variation in stress–stretch curves resulting from changes in the most influential input parameters. For elastin stiffness and collagen stiffness, decreasing the reference value by 10% and 20% of the literature-reported range resulted in negative stiffness values. Therefore, the selected values were adjusted to remain positive. Similarly, for κ_{op}, a 10% and 20% increase resulted in no fiber dispersion, as it exceeded the upper limit of 0.5. Consequently, the values were slightly adjusted to stay within the valid range, allowing for fiber dispersion. Table E.5 contains all the input values selected to run the 44 simulations.

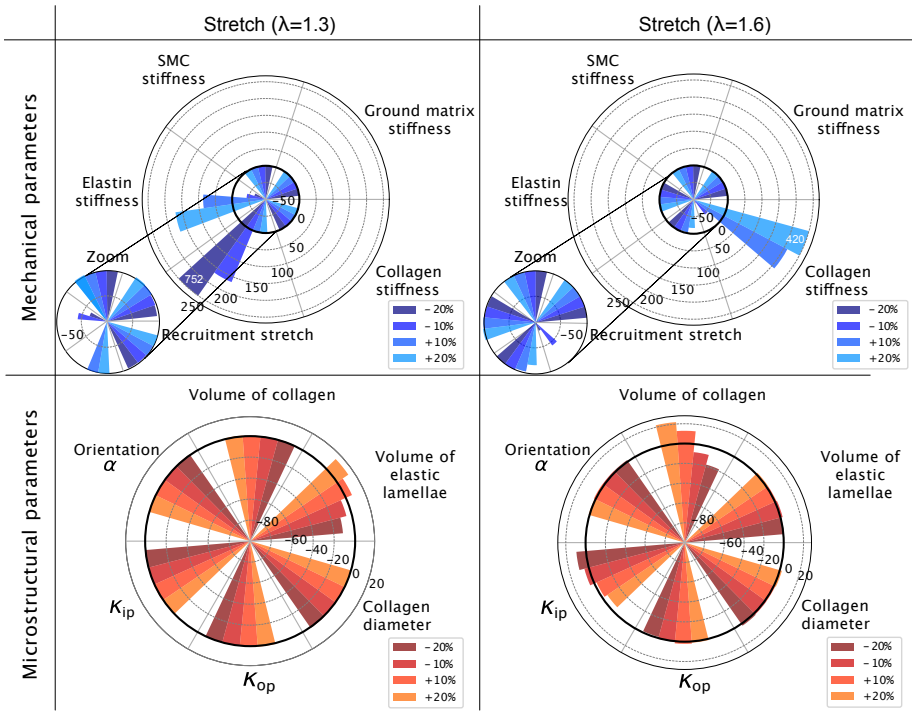


Fig. 10: Parameter sensitivity analysis of mechanical and microstructural input parameters. Biaxial virtual tensile tests were performed, and the resulting circumferential stress–strain curves were analyzed. Tangential stiffness was evaluated at 30% nominal strain (toe region) and 60% nominal strain (exponential region), and the results were compared to the reference RVE, indicated by the black 0% line. The relative increase or decrease in tangential stiffness is illustrated with respect to the reference RVE in percent. Values are capped at 250% for visualization purposes; however, values exceeding this threshold are indicated in white.

For the mechanical parameters, an increase in elastin stiffness and a decrease in recruitment stretch values had the highest impact at low strain (Fig. 11.a). Indeed, as long as the collagen fibers are not recruited, elastin dominates the stress-strain curve response, leading to a 171% increase in stiffness for a 20% increase in elastin stiffness and a reduction of -65% for a 20% decrease. A decrease in recruitment stretch value caused an earlier onset of the exponential behavior (Fig. 11.a). At -20% of the recruitment stretch value,

the tangential stiffness increased by 752%; however, for visualization purposes, it was limited to a 250% increase in the plot ((Fig. 10). At higher strain, collagen stiffness had the greatest influence on the tangential stiffness. A 20% increase in collagen stiffness resulted in a 420% rise in tangential stiffness. Contrarily, a 20% decrease in collagen stiffness reduced tangential stiffness of -10% of the reference RVE value. The stiffness of the ground matrix and smooth muscles cells had almost no impact on the overall stress-strain curve as their stiffness was significantly lower than the one of elastin and collagen.

In comparison, the microstructural parameters had a lesser impact on the tangential stiffness of the stress-strain curve. At low strain, the volume fraction of elastic lamellae played the most significant role ((Fig. 11.b). An 20% increase in volume fraction raised the tangential stiffness of 13%. At higher strain, the collagen volume fraction and in-plane collagen fiber dispersion (κ_{ip}) had a more dominant influence ((Fig. 11.b). A 20% increase in collagen volume fraction results raised the tangential stiffness of 22%. In the contrary, a 20% increase in κ_{ip} decreased the tangential stiffness to -6%.

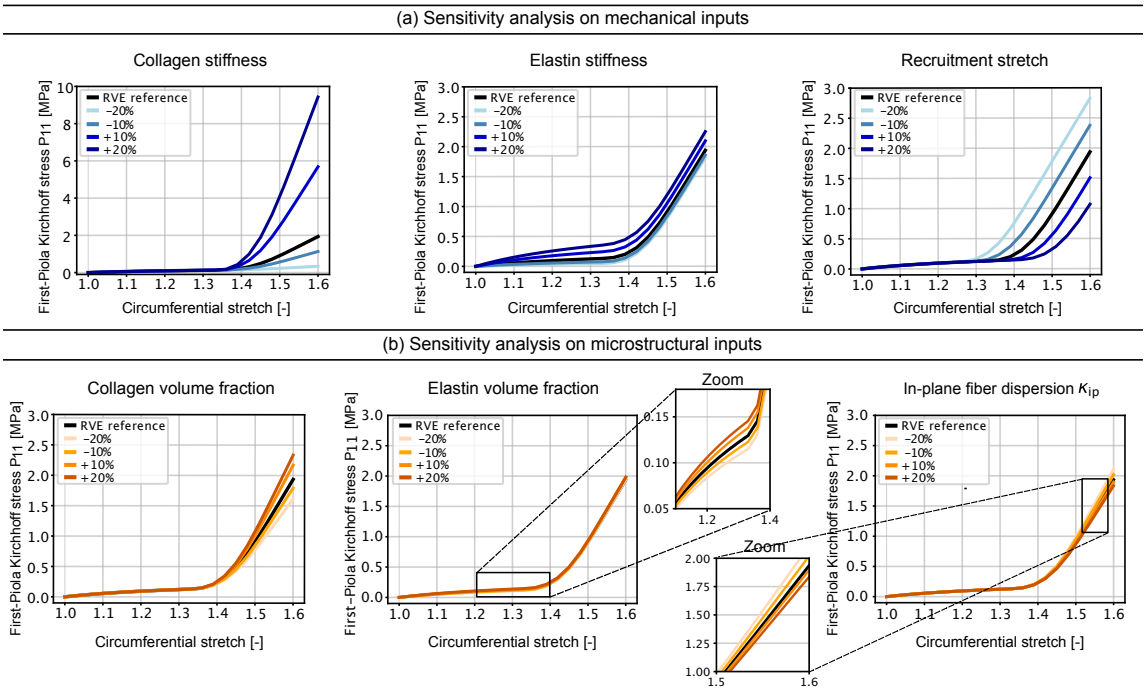


Fig. 11: (a) Stress–stretch curves in the circumferential direction illustrating the influence of key mechanical input parameters (i.e. collagen stiffness, elastin stiffness and recruitment stretch) on the overall mechanical response. (b) Stress–stretch curves in the circumferential direction illustrating the influence of key microstructural input parameters (i.e. collagen and elastin volume fractions, and collagen in-plane fiber dispersion κ_{ip}) on the overall mechanical response. Each parameter was varied from its reference value by −20%, −10%, +10% and +20% relative to its range reported in literature. The black thick line is the reference RVE.

3.3. Model validation

To validate the model, uniaxial tensile tests were performed on descending thoracic porcine aorta samples (i.e. intercostals four until seven). Porcine aortas were obtained from the WestVlees slaughterhouse (Belgian Pork Group, Westrozebeke, Belgium) and were cut in dogbone shaped samples according to the C^{4}Bio protocol [60], along the circumferential and axial direction. The adventitial layer was removed by carefully peeling it off. For each direction, seven samples from seven different pigs were tested. More details on the materials and methods regarding the mechanical tests can be found in the Appendix D.

By performing virtual uniaxial tensile tests on the reference RVE model with a 60% stretch (i.e. chosen to match the maximum stretch level reached in the experimental mechanical tests) and comparing the resulting

homogenized First Piola-Kirchhoff stress with the experimental data, one can observe that the model stress-strain curves are within the experimental range (Fig. 12). The circumferential RVE stress tends towards the upper limit of the experimental range, whereas the axial RVE stress tends towards the lower limit of the experimental range.

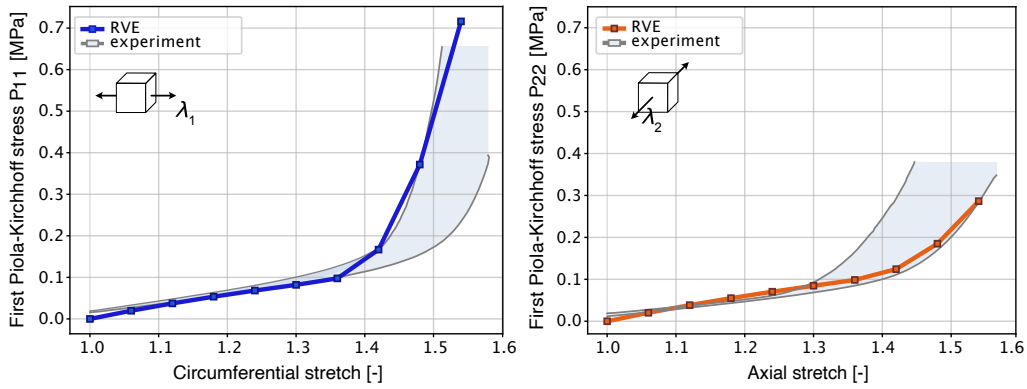


Fig. 12: Experimental validation of the RVE model by performing uniaxial tensile tests in both circumferential and axial direction on porcine thoracic descending aortas, where the adventitial layer was removed. The greyed region represents the variability across the seven samples tested.

3.4. Role of RVE Components in the Macroscopic Stress Response

To better understand the influence of each microstructural component from the RVE model on the overall macromechanical response, equations (14-15) were used to plot their individual contributions (Fig. 13). A virtual biaxial test was performed on the reference RVE configuration. The collagen fibers played a predominant role at higher stretch and provide the non-linear and exponential behavior to the stress-stretch curve. Since smooth muscle cells, elastin struts, and interlamellar elastin fibers have a low volume percentage in the RVE model, their mechanical contributions were combined and are represented in dark red. In the axial direction, the collagen fibers played a less dominant role since collagen fibers are preferentially aligned along the circumferential direction.

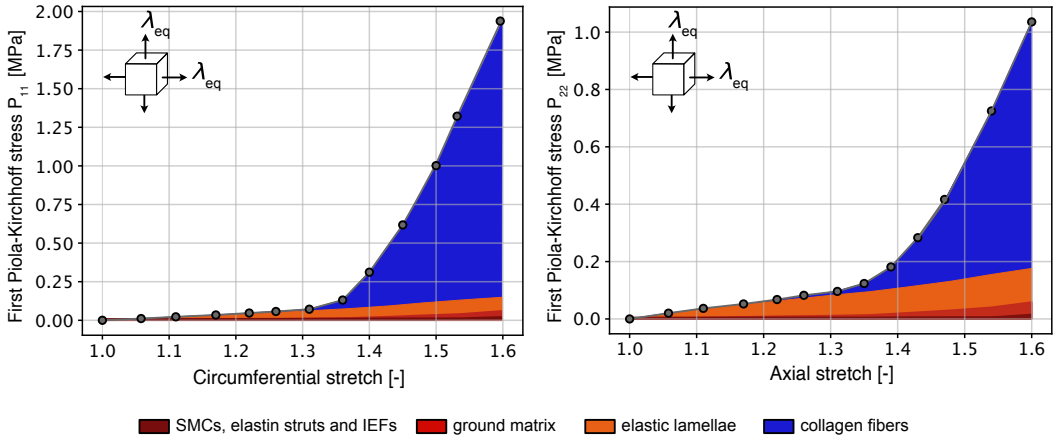


Fig. 13: The circumferential and axial stress-stretch curves are decomposed into their microstructural components, showing the individual contributions of every microstructural component to the overall mechanical behavior, such as the smooth muscle cells (SMCs), elastin struts, interlamellar elastic fibers (IEFs), ground matrix, elastic lamellae and collagen fibers.

3.5. Impact of microstructural changes

As the RVE model script is fully parametrized, we can easily generate a different RVE microstructure by modifying the microstructural inputs. To illustrate this, two RVEs with different elastin and collagen volume fractions were constructed. RVE_1, the reference model, is composed of 30% of collagen fibers and 50% of elastic lamellae as mentioned in Table 1, and represents a porcine thoracic descending aorta. RVE_2 is similar to RVE_1, except that the collagen content was increased to 55% and the elastic lamellae decreased to 25%. A 20%-40% elastin content, typically corresponds to infrarenal aortas [34]. All other microstructural components (i.e. elastin struts, smooth muscle cells...) were kept constant (Table 1). RVE_1 consisted of 109,245 truss elements representing the collagen fibers, while RVE_2 contained 201,520 truss elements. Virtual equibiaxial tests up to 60% nominal strain were performed on both RVEs (Fig. 14.a). RVE_2 exhibited a stiffer behavior towards higher stretches, due to its higher collagen content. However, it exhibited a slightly softer behavior in the toe region as the elastin content was decreased. Additionally, parameter fitting was performed to identify the five parameters of the GOH model (Table 4). Figure 14.b shows that the fit was better in the axial direction than in the circumferential direction. Indeed, the GOH model had difficulties in accurately capturing the long toe region present in both the experimental and the RVE model.

Table 4: Gasser-Ogden-Holzapfel model parameters identified for the two different RVEs.

Model	C_{10} $[MPa]$	k_1 $[MPa]$	k_2 $[-]$	κ $[-]$	α $[rad]$	**RMSE**
RVE_1	0.014	0.17	1.65	0.055	0.26	0.05
RVE_2	0.001	0.4	1.94	0.055	0.26	0.09

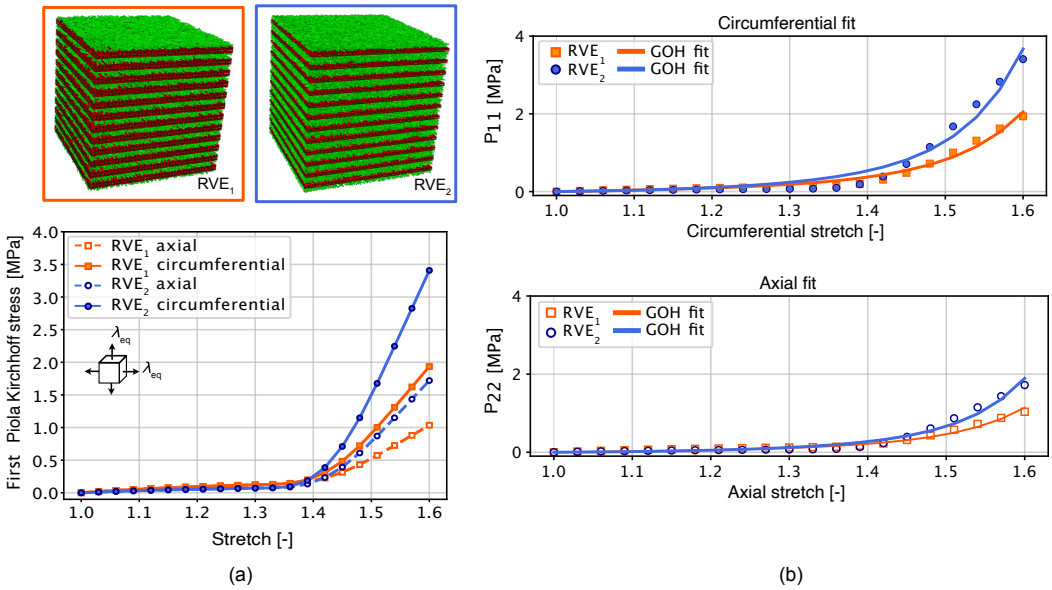


Fig. 14: (a) Two different RVE models with size $360^3 \mu m^3$ were created and tested virtually with a biaxial tensile test. RVE_1 is composed of 30% collagen and of 50% elastic lamellae, representing a thoracic descending aorta, whereas RVE_2 is composed of 55% collagen and 25% elastic lamellae, representing a infrarenal aorta [34]. All other components are kept the same as defined in Tables 1, 2 and 3. RVE_2 exhibits a stiffer behavior towards higher stretches. (b) The Gasser-Odgen-Holzapfel (GOH) model was fitted to the data to define the five different parameters for both RVEs.

C_{10} was logically higher for RVE_1 than RVE_2 since it represents the shear modulus of the ground matrix

and elastin, which is more abundant in the former. In contrast, k_1 and k_2, which correspond to the fiber stiffness and fiber non-linearity, respectively, are higher in RVE_2 than in RVE_1 due to the higher collagen fiber content in RVE_2. The fiber dispersion κ and mean fiber angle α remain identical in both RVE models since the fiber orientation was not changed between RVE_1 and RVE_2.

Figure 15 presents the decomposition of the stress–stretch curve obtained from both the RVE and GOH models, allowing for a comparison of the contributions from different components. Specifically, it illustrated how much of the curve was attributed to the anisotropic response of the collagen fibers versus the isotropic response of the ground matrix, elastic lamellae, smooth muscle cells (SMCs), elastin struts, and interlamellar elastin fibers (IEFs). In the GOH model, the isotropic matrix contribution was minimal, reaching only about 0.001 MPa. In contrast, the corresponding isotropic contribution in the RVE model was significantly larger, accounting for up to 0.12 MPa of the total stress–stretch response.

Moreover, the RVE stress–stretch curve enabled the identification of the individual contributions of each component within the ground matrix, including the elastic lamellae, smooth muscle cells (SMCs), elastin struts, interlamellar elastin fibers (IEFs), and the remaining matrix material. Additionally, the RVE model provided insight into the specific stretch experienced by the collagen fibers, as well as the SMCs. It is particularly important to focus on the stretch experienced by smooth muscle cells (SMCs), as they are often connected to adhesion molecules such as integrins and cadherins that are responsible for cell-cell and cell-matrix interactions. Depending on the magnitude and nature of the stretch, these molecules initiate intracellular signaling pathways that regulate various SMC functions, including proliferation, migration, and phenotypic switching [61, 62].

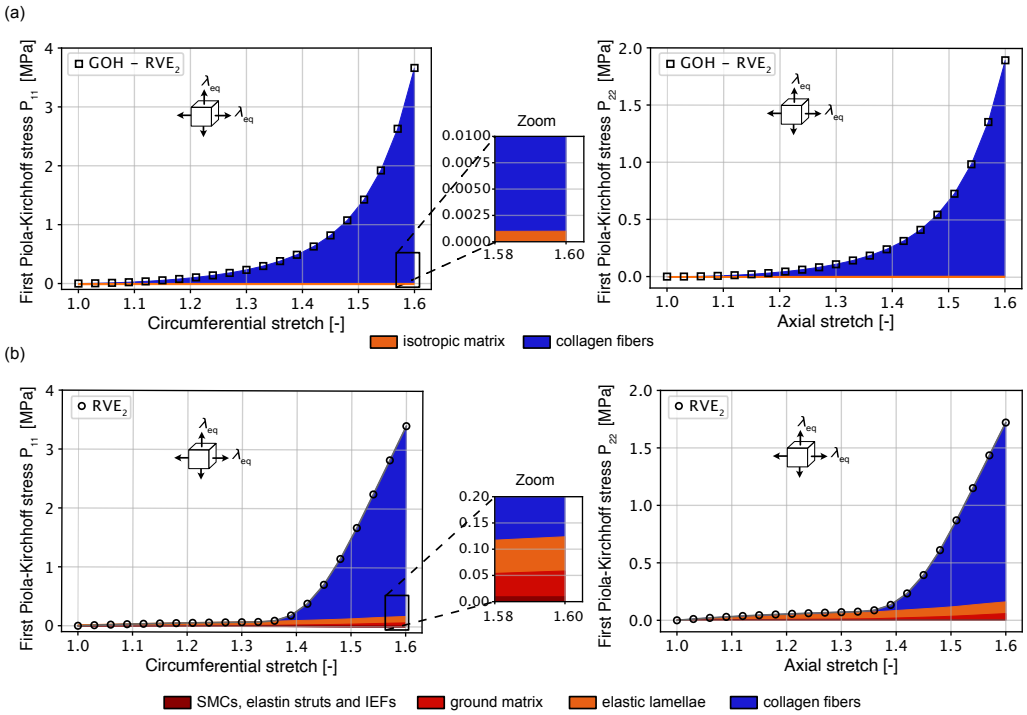


Fig. 15: (a) Decomposition of the GOH stress-stretch curve, obtained via parameter fitting of RVE_2, into an isotropic contribution (the matrix) and an anisotropic contribution (the collagen fibers). (b) Decomposition of the RVE_2 stress-stretch curve into an isotropic response from the ground matrix, elastic lamellae, smooth muscle cells (SMCs), elastin struts, and interlamellar elastin fibers (IEFs), and an anisotropic response from the collagen fibers.

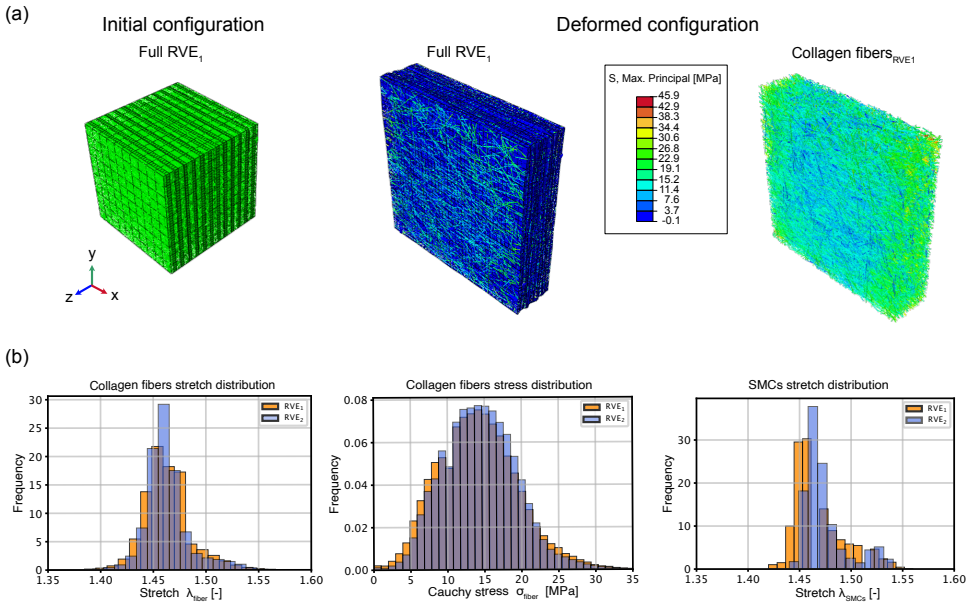


Fig. 16: (a) A biaxial test with 1.6 stretch applied to the RVE, showing the different fiber stresses in the deformed configuration. (b) Plots of collagen fiber stretch and stress for the two RVEs as well as the SMCs stretch.

Figure 16.a illustrates how the RVEs deform under 60% strain. Despite the periodic boundary conditions, the collagen fibers exhibit higher stresses near the boundary of the RVE. Figure 16.b shows the SMCs stretch distribution in both RVEs simulation as well as the collagen stretch and stress distributions. Although the virtual biaxial test applied a 60% stretch, most individual fiber stretches did not reach such high values. Moreover, the fiber stress distribution indicated that some fibers experienced zero stress, as their stretch levels remained below the assigned recruitment stretch value. Similar to the collagen fibers, the stretch distribution of the SMCs revealed lower stretch values than the 60% applied stretch.

4. Discussion

In this study, we developed a microstructure-based representative volume element model of arterial tissue, incorporating key structural components, in casu elastic lamellae, elastin fibers, collagen fibers, and smooth muscle cells. Using the embedded element technique, we were able to discretely represent the microstructure of the porcine aortic medial layer. The microstructural inputs were derived from literature data as multiple imaging techniques are required to visualize the various structural components due to their differing scales. These techniques include CECT, classical 2D histology, multiphoton microscopy, and SEM. A limitation of this approach is that the data were obtained from various species and different arteries, such as the aortas and carotid arteries of rats, pigs, and humans. Consequently, we assumed that values reported for rats and humans were reasonably comparable to those of porcine arteries, allowing us to approximate certain microstructural properties when specific porcine data were unavailable. In this study, the aorta was chosen because it is extensively studied in the literature. However, many cardiovascular diseases occur in other arteries, such as the coronary and carotid arteries, particularly in the development of atherosclerosis. Moreover, investigating aortic aneurysms or dissections presents an interesting direction for future work, particularly by constructing distinct RVEs for different regions of the aortic wall to capture localized pathological changes. To effectively use the RVE model as a tool for understanding disease progression, it is essential to obtain accurate microstructural data for the arteries of interest. This highlights the importance of imaging the microstructure of arteries in high detail and combining several imaging modalities to capture all the necessary information.

Our RVE model provides a more advanced and detailed representation of arterial tissue microstructure compared to existing models in the literature. We discretely incorporate multiple medial lamellar units, capturing key microstructural components with greater fidelity. To the best of our knowledge, no previously proposed arterial RVE includes such a comprehensive set of microstructural components. However, further refinement is possible by including additional components, such as Glycosaminoglycans (GAGs) and their swelling behavior. GAGs are typically bound to core proteins to form proteoglycans, which contribute to the structural integrity and function of blood vessels [63]. These molecules play a vital role in various vascular events, such as the regulation of vascular permeability, lipid metabolism, hemostasis, and thrombosis, but also interact with vascular cells, growth factors, and cytokines to modulate cell adhesion, migration, and proliferation [64]. It could be interesting to implement such GAGs complex and their responses into the RVE model such as described in [65, 66].

In this study, we investigated the size convergence of our RVE model and demonstrated that the macroscopic behavior was dependent on the selected size up to a certain threshold of 360 μm, beyond which consistent mechanical behavior was observed regardless of further size increases. This indicates that eleven medial lamellar units are required in our model to obtain a representative mechanical behavior. A medial lamellar unit is defined as two elastic lamellae with an interlamellar space containing collagen, smooth muscle cells, and elastin fibers. To provide context, a porcine medial aorta typically consists of 70 elastic lamellae and is on average 1400 μm thick [25]. Moreover, we analyzed the mesh convergence of the host mesh by assessing five different mesh sizes. While the impact of the mesh size was less than 0.2% between mesh 1 and mesh 7 (the most refined) at low stretches in the toe region, it increased up to 2% as the stretch increased. This is likely due to the fiber mesh discretization, which was kept constant in this analysis and should potentially be varied in accordance with the host mesh size. In this context, it is also worth noting that inadequate discretization of the fiber mesh may have contributed to localized stress concentrations near the boundaries of the RVE. In our model, collagen fibers were divided into elements with a length of 18 μm, which corresponds to approximately 5% of the RVE size. A mesh sensitivity analysis on the collagen fiber mesh should be conducted in future work to determine the optimal discretization size and minimize localized stress artifacts. Indeed, when the collagen fibers were removed from the RVE model, no stress localization was observed. Additionally, the use of a quadratic material model for the collagen fibers may amplify stress concentrations, particularly in regions with high deformation gradients.

By assigning mechanical properties obtained from the literature, our model successfully replicated the experimental mechanical behavior observed in uniaxial tensile tests on porcine aortic tissue. The fit between the RVE model and the experimental data could be further improved through a proper calibration step using additional experimental samples and by performing more physiologically relevant biaxial tensile tests [67]. Moreover, no pre-stretch was applied to the RVE model. To better replicate the in vivo pre-strains, this aspect could be explored in future work. Beyond validating the model's ability to reproduce experimental data, we conducted a parameter sensitivity analysis to evaluate the influence of mechanical and microstructural properties on the overall mechanical response of the RVE. However, our local sensitivity analysis focused only on evaluating the impact of each individual parameter on the mechanical behavior of the RVE. This provided insight into the most influential parameters, namely the mechanical properties assigned to the RVE components and the volume percentages of elastin and collagen present. A next step would be to perform a global sensitivity analysis and explore interactions between multiple parameters using a variance-based method, such as the Sobol method, to better understand their combined effects on the overall mechanical behavior [68]. As this would require a large number of simulations, it might be necessary to define a surrogate model for this step, as done for example in [69].

Our model allows for the quantification of how each individual constituent deforms during the overall deformation process. We demonstrated that the degree of stretch varies across collagen fibers and SMCs, with average stretch levels significantly lower than the macroscopic stretch applied to the RVE. Looking ahead, the model could be extended to explicitly incorporate adhesion molecules such as integrins and cadherins,

which play a critical role in mechanotransduction and cellular response to mechanical stimuli. This is particularly important when studying the pathophysiological processes involved in ECM growth and remodeling, as it would provide valuable insights for integration into cell-scale models that include gene regulatory networks [14]. Building on this, the RVE framework could be extended in a full multiscale approach by coupling it with such cell-scale models [14, 70]. For instance, a gene regulatory network could inform the RVE about changes in matrix composition (e.g., collagen, elastin). In turn, the RVE's homogenized mechanical response could feed back into a tissue-scale model, enabling dynamic, bidirectional interactions across scales and offering a more comprehensive understanding of tissue adaptation and remodeling. However, there is room for improvement in the material models selected for elastin and SMCs. When analyzing the contribution of different RVE components to the macroscopic stress response, we found that collagen and elastic lamellae played a dominant role, while SMCs, interlamellar elastin fibers, and elastin struts had a minimal impact. This can be explained by the difference in stiffness between collagen and the other RVE components, as well as the material models chosen. Neo-Hookean material models were initially selected for their simplicity and computational efficiency, which allowed us to focus on establishing and validating the RVE framework. However, this simplification limits the ability to capture the viscoelastic behavior typical of soft biological tissues. In the current implementation, collagen fibers are the only components contributing to the non-linear and anisotropic mechanical behavior. In the future, it could be valuable to adapt the material models of elastic lamellae and SMCs, and to explore alternative formulations such as Mooney–Rivlin or Ogden models, or even to develop a custom user-defined material model tailored to these components. Indeed, elastic lamellae also exhibit a certain degree of tortuosity, which can be visualized and quantified using CECT [25]. Incorporating this feature into the model could be beneficial, potentially by implementing a material model similar to that of collagen, with a recruitment stretch principle. Additionally, SMCs exhibit both active and passive mechanical behavior, which could be worth exploring further in a more complex material model than the neohookean model [71, 72].

Thanks to the parametrized Python code that enables the generation of the RVE geometry, we were able to easily modify the microstructural parameters by adjusting, in this study, the volume percentages of elastin and collagen. We demonstrated that our RVE model was sensitive to these changes, as it produced different mechanical behavior for the two RVE geometries. We used the GOH model to identify the five homogenized parameters for both RVEs. Only the material parameter C_{10} linked to the ground matrix (i.e. elastin, SMCs...) and the two parameters k_1 and k_2 linked to the collagen fiber stiffness and fiber non-linearity differed from RVE 1 to RVE 2. The other parameters, related to collagen fiber orientation, were not impacted, as the same orientation and dispersion were maintained from RVE 1 to RVE 2. However, the fit between the GOH stress-strain curve and the RVE model was not perfect, especially in the long toe region, which was observed both experimentally and in the RVE model. The lack of fit was more pronounced for RVE 2, which deviates from the microstructure of a healthy artery. This suggests that there is a need in using different constitutive model formulations, particularly when modeling altered or diseased arterial microstructures. One potential solution could be automated model discovery, where a neural network identifies the most suitable constitutive model [73, 74]. Recent advances even enable the identification of complex, time-dependent material behaviors such as viscoelasticity using inelastic Constitutive Artificial Neural Networks (iCANNs) [75]. Another approach is to explore poro-visco-hyperelastic models, which account for the coupled effect of fluid transport, viscoelasticity, and non-linear elasticity, offering a more physiologically representation of the tissue-scale behavior [76, 77].

5. Conclusion

In conclusion, we presented a microstructurally detailed RVE model for the porcine aortic medial layer based on information from multiple imaging modalities. By incorporating elastic lamellae, elastin fibers, collagen fibers, and SMCs representing the microstructural information obtained from the literature as faithfully as possible, we were able to successfully replicate experimentally obtained stress-strain curves. The model's size convergence analysis demonstrated that at least eleven medial lamellar units are required for a representative mechanical response. Mesh convergence and sensitivity analyses further highlighted the

importance of selecting appropriate microstructural and material parameters. Our results demonstrated that collagen fibers have the most impact on the overall mechanical behavior due to their significantly greater stiffness and specific material model. Moreover, our model allows to quantify how each individual constituent deforms during the overall deformation, and we showed how the de degree of stretch level varies over the collagen fibers, whereby the average stretch level is significantly below the macroscopic stretch of the RVE. Future refinements could involve enhancing the material models for elastic lamellae and SMCs to account for lamellae tortuosity and the more complex active and passive mechanical behavior of SMCs. Thanks to its fully parameterized code, this RVE framework provides a valuable tool for understanding arterial microstructure-function relationships, with potential applications in cardiovascular disease research and computational modeling of arterial pathologies.

Acknowledgments

This research benefited from the help of Laurent Delannay and Guillaume Hanon for the periodic bounadry implementation. M. Pétré acknowledges the Flanders Community of Belgium in the framework of a FWO Project grant (G088020N) and a FWO-SB Mandate grant (1S64923N). N.Famaey acknowledges KU Leuven's Bijzonder Onderzoeksfonds for supporting the Core Facility FIBEr where the mechanical tests were performed (3E210166 KERNFAC FIBER).

Supplementary materials

The source data and code are available in KU Leuven's research data repository: https://rdr.kuleuven.be/previewurl.xhtml?token=31b68606-d63d-4b71-bea1-927c0d27cca9.

Appendix A. Generation of the RVE

To generate the RVE geometry, we started by defining the domain size, L_{cube}. The interlamellar space was set to $15\mu m$, and the volume fraction V_{EL} of the elastin lamellae is fixed at 50%. For an RVE of size 120 μm, this results in four elastic lamellae. The elastic lamellae are modeled as shell elements, initially created as 2D planes in Pyvista. Later, in Abaqus, a thickness was assigned to these planes, growing outward from their mid-surfaces. The thickness of the elastic lamellae is defined as:

$$T_{EL} = V_{EL} * L_{cube}/n_{planes} \tag{A.1}$$

To impose periodicity, the first plane is positioned at $z_{coord} = 15\mu m$, where it it grows symmetrically by 7.5 μm on each side. This ensures that the first and last interlamellar spaces each have a thickness of $7.5\mu m$, so that when stacked, they form a complete interlamellar space of $15\mu m$ (Fig. 5). The z-coordinates of the subsequent elastic lamellae are determined by incrementally adding a spacing $T_{spacing}$, which is set to $30\mu m$ in this case (see algorithm 1). Finally, the z_{min} and z_{max} coordinates of the interlamellar space, where fibers and SMCs reside, can be determined (Fig. 5).

Algorithm 1 : Generation of elastic lamellae

Input: L_{cube}, V_{EL}, n_{planes}, T_{EL}, $T_{spacing}$
Output: N_{EL}

1: Define thickness of elastic lamellae: $T_{EL} = V_{EL} * L_{cube}/n_{planes}$
2: Define $z_{coord} = 0.015$ of 1^{st} plane
3: **for** $i = 1, \ldots n_{planes}$ **do**
4: $\quad z_{coord} += T_{spacing}$
5: $\quad$ Create plane with length L_{cube} at updated z_{coord}
6: $\quad$ Define z_{min} and z_{max} as an array for each interlamellar space
7: **end for**

Once the elastic lamellae were created, the corresponding z_{min} and z_{max} coordinates of each interlamellar space are known. For each interlamellar space, a fiber orientation angle is first selected from both the in-plane and out-of-plane distributions, alternating between $+\alpha$ and $-\alpha$ (see algorithm 2). The fiber direction vector is then computed. Next, a random nucleation point r_0 is generated within the boundaries of the interlamellar space domain. The fiber's endpoint r_1 is determined by adding to r_0 the fiber length multiplied by the orientation vector. Then, r_1 is checked to see if it lies outside the interlamellar space boundary. If r_1 remains within the boundary, the fiber is added to the pool, and the steps are repeated until the current volume fraction $VF_{current}$ reaches the target fiber volume fraction V_f. If r_1 extends beyond the boundary, the intersection point with the boundary is determined, and r_1 is set at this intersection. A second fiber is then generated symmetrically from r_1 with the remaining length to ensure the total fiber length equals L_f. Both fibers are added to the pool and the steps are repeated until $VF_{current}$ equals V_f.

Algorithm 2 : Generation of the collagen fiber networks

Input: L_{cube},V_F, d, z_{min}, z_{max}
Output: $\forall k = 1, \dots N_{fibers}$, (r_0^k, r_1^k)

for $n = 1, ..., n_{planes}$ **do**
  $VF_{current} = 0$
  $Lf = 0.12$
  $count = 0$
  while $VF_{current} < V_F$ **do**
    Sample out-of-plane angle value θ_k from the von Mises distribution (Eq. 4)
    if $count = odd$ **then**
      Sample in-plane angle value ϕ_k from the von Mises distribution (Eq. 3), centered on $+\alpha$
    else
      Sample in-plane angle value ϕ_k from the von Mises distribution (Eq. 3), centered on $-\alpha$
    end if
    Calculate the fiber direction $N(\Phi, \Theta)$ (Eq. 1).
    Initiate random initial fiber nucleation point $r_0 = [x_0, y_0, z_0]$, with $x_0 \in [0, L_{cube}]$, $y_0 \in [0, L_{cube}]$, $z_0 \in [z_{min}^p, z_{max}^p]$.
    Compute end point of fiber $r_1 = r_0 + L_{fiber} * N(\Phi, \Theta)$
    Check if r_1 is located outside of cube boundaries
    if $r_1 \notin [(0, L_{cube}), (0, L_{cube}), (z_{min}^p, z_{max}^p)]$ **then**
      Define r_1^{new} the point located at the intersection with the boundaries of the cube
      $Fiber += (r_0, r_1^{new})$
      Compute $L_{fiber} = \sqrt{(x_1^{new} - x_0)^2 + (y_1^{new} - y_0)^2 + (z_1^{new} - z_0)^2)}$
      $VF_{current} += L_{fiber} \frac{\pi}{4} d^2$
      Define r_0^{new} the symmetrical point from r_1^{new}
      Compute the remaining length $L_{fiber}^{new} = L_f - L_{fiber}$
      $r_2 = r_0 + L_{fiber}^{new} * N(\Phi, \Theta)$
      if $r_2 \notin [(0, L_{cube}), (0, L_{cube}), (z_{min}^p, z_{max}^p)]$ **then**
        Repeat step 16-19
      else
        $Fiber += (r_0^{new}, r_2)$
        $VF_{current} += L_{fiber}^{new} \frac{\pi}{4} d^2$
      end if
    else
      $Fiber += (r_0, r_1)$
      $VF_{current} += L_F \frac{\pi}{4} d^2$
    end if
  end while
end for

Appendix B. Abaqus implementation of PBC

The periodic boundary conditions (Eq. 11-13) can be written as:

$$u_i^{(R)} - u_i^{(L)} = \overline{\epsilon}_{ij}(x_j^{(R)} - x_j^{(L)}) = \overline{\epsilon}_{ij}(x_j^{(M_1)} - x_j^{(O)}) \tag{B.1}$$

$$u_i^{(F)} - u_i^{(Bk)} = \overline{\epsilon}_{ij}(x_j^{(F)} - x_j^{(Bk)}) = \overline{\epsilon}_{ij}(x_j^{(M_2)} - x_j^{(O)}) \tag{B.2}$$

$$u_i^{(T)} - u_i^{(Bm)} = \overline{\epsilon}_{ij}(x_j^{(T)} - x_j^{(Bm)}) = \overline{\epsilon}_{ij}(x_j^{(M_3)} - x_j^{(O)}) \tag{B.3}$$

where the difference between the coordinates of corresponding nodes on the right and left boundaries is equal to the difference between the coordinates of master node 1 and the origin, and where $x_j^{(O)} = 0$. Similarly, this applies to the top and bottom boundaries, as well as the back and front boundaries, with the corresponding relationships for master node 2 and the origin, and master node 3 and the origin.

The displacement of the master nodes can then be expressed in terms of the macroscopic strain tensor, which is assumed to be known:

$$u_i^{(M_1)} = \overline{\epsilon}_{ij} x_j^{(M_1)} \tag{B.4}$$

$$u_i^{(M_2)} = \overline{\epsilon}_{ij} x_j^{(M_2)} \tag{B.5}$$

$$u_i^{(M_3)} = \overline{\epsilon}_{ij} x_j^{(M_3)} \tag{B.6}$$

In Abaqus, constraints between degrees of freedom, equations (11-13), are implemented using the keyword ∗EQUATION:

```
*EQUATION
3
Right, 1, 1, Left, 1, −1, M1, 1, −1
3
Right, 2, 1, Left, 2, −1, M1, 2, −1
3
Right, 3, 1, Left, 3, −1, M1, 3, −1
3
Front, 1, 1, Back, 1, −1, M2, 1, −1
3
Front, 2, 1, Back, 2, −1, M2, 2, −1
3
Front, 3, 1, Back, 3, −1, M2, 3, −1
3
Top, 1, 1, Bottom, 1, −1, M3, 1, −1
3
Top, 2, 1, Bottom, 2, −1, M3, 2, −1
3
Top, 3, 1, Bottom, 3, −1, M3, 3, −1
```

The displacements of the master nodes, equations (B.4)-(B.6), is prescribed via ∗BOUNDARY:

```
*BOUNDARY
Node i, 1, 3, 0
M1, 1, 1, u1^(M1)
M1, 2, 2, u2^(M1)
M1, 3, 3, u3^(M1)
M2, 1, 1, u1^(M2)
```

$\mathtt{M_2}, \mathtt{2}, \mathtt{2}, u_2^{(M_2)}$
$\mathtt{M_2}, \mathtt{3}, \mathtt{3}, u_3^{(M_2)}$
$\mathtt{M_3}, \mathtt{1}, \mathtt{1}, u_1^{(M_3)}$
$\mathtt{M_3}, \mathtt{2}, \mathtt{2}, u_2^{(M_3)}$
$\mathtt{M_3}, \mathtt{3}, \mathtt{3}, u_3^{(M_3)}$

where the displacement of Node i is fixed to prevent any rigid body translation.

Appendix C. Homogenization using traction fields

One way to retrieve the overall macroscopic stress is to know the traction field on the surface of interest [16, 55, 54, 56]. Indeed, the microscopic stress can be written as follows:

$$\sigma_{ij} = \sigma_{ik}\delta_{jk} = \sigma_{ik}\frac{\delta x_j}{\delta x_k} \tag{C.1}$$

where δ_{ij} is the Kronecker's symbol. It follows that the integral of the microscopic stress can be rewritten as:

$$\int_V \sigma_{ij}\, dV = \int_V \sigma_{ik}\frac{\delta x_j}{\delta x_k}\, dV \tag{C.2a}$$

$$= \int_V \frac{\delta}{\delta x_k}(\sigma_{ik}x_j)\, dV - \int_V \underbrace{\frac{\delta \sigma_{ik}}{\delta x_k}}_{=0} x_j\, dV \tag{C.2b}$$

$$= \int_{\delta V} \sigma_{ik}x_j n_k\, dA \tag{C.2c}$$

$$= \int_{\delta V} t_i x_j\, dA \tag{C.2d}$$

The second equality arises from the application of the product rule. The second term on the right-hand side becomes zero due to mechanical equilibrium. The third equality is derived using the divergence theorem, while the fourth equality follows from Cauchy's law $t_i = \sigma_{ij}n_j$. Similarly, one can express:

$$\int_V \sigma_{ij}\, dV = \int_{\delta V} t_j x_i\, dA \tag{C.3}$$

Since the stress tensor is symmetric, it follows that:

$$\int_V \sigma_{ij}\, dV = \frac{1}{2}\int_{\delta V} (t_i x_j + t_j x_i)\, dA \tag{C.4}$$

Expression (C.4) is preferred over expression (C.3) as it ensures that the macroscopic stress calculated from the surface traction is symmetric. In Abaqus, the traction fields can be easily obtained by extracting the reaction forces at the master nodes used in the simulation.

Appendix D. Experimental mechanical tests

Uniaxial tensile tests were performed on descending thoracic porcine aorta samples to validate the RVE model. Within 24 hours after harvesting, all samples were preserved at -80°C through a snap freezing step in -75°C isopentane before being used for mechanical testing [78]. On the day of the experiment, the samples were thawed at room temperature and their thickness was measured with a micro-laser scanner (Gocator 2300, LMI technologies, Canada). Then, the samples were tested with a Messphysik-Zwick/Roell uniaxial tensile testing machine (Zwick/Roell, Germany) under displacement control. The samples were

mounted using metallic toothed clamps and were placed in a PBS liquid bath at 37°C to replicate the in vivo conditions. A preload of 0.1 N was applied to avoid sagging of the sample. Ten loading cycles were performed with a total displacement of 16 mm, followed by a final cycle in which the sample was loaded until failure. Fourteen samples, each from a different pig, were tested in uniaxial tension in both directions (seven samples per direction). A speckle pattern with graphite powder was deposited on the sample for strain mapping with 2D digital image correlation (DIC) using the software VIC-2D (Correlated Solutions, USA). The area of interest to compute the correlation was defined by the neck region of the dogbone sample in its reference configuration. A subset of 65 pixels and a step size of 7 pixels were used. Thanks to the VIC-2D DIC analysis, the spatial distribution of the Green-Lagrange strain components along the principal experimental direction was computed. The 1^{st} Piola-Kirchhoff stress P was computed by dividing the reaction forces measured $RF(t)$ by the undeformed cross-sectional area A_0. Due to the snap-freezing step used for sample preservation, it is unlikely that the SMCs remained viable. However, while their active contractile function is likely lost, their passive mechanical properties are still expected to contribute to the overall tissue response.

Appendix E. Parameter Sensitivity Analysis

The parameter sensitivity analysis was performed on the following mechanical and microstructural input parameters described in Table E.5. For each parameter, we considered the range reported in the literature, computing 10% and 20% of this range. We then applied a decrease and increase of 10% and 20% to the simulated value chosen for the reference RVE. In total, 44 simulations were performed. The values in bold were adapted to maintain a positive stiffness for elastin and collagen and to ensure that $\kappa_{op} \in [0, 0.5]$ remains within a valid range for fiber dispersion.

Table E.5: Input parameters selected for the parameter sensitivity analysis. The values in bold were adapted to maintain a positive stiffness for elastin and collagen and to ensure that $\kappa_{op} \in [0, 0.5]$ remains within a valid range for fiber dispersion.

Mechanical parameters	**Reference value**	**-20%**	**-10%**	**10%**	**20%**
Ground matrix stiffness [kPa]	8.04	6.45	7.25	8.83	9.63
SMC stiffness [kPa]	8	8.70	18.35	37.65	47.30
Elastin stiffness [MPa]	0.1	**0.03**	**0.05**	0.2	0.3
Recruitment stretch [start - end]	[1.323-1.523]	[1.24-1.43]	[1.28-1.48]	[1.36-1.57]	[1.40-1.62]
Collagen stiffness [MPa]	54.3	**4.70**	**29.30**	170.83	287.36
Microstructural parameters	**Reference value**	**-20%**	**-10%**	**10%**	**20%**
Volume of elastic lamellae [%]	50	43	46.5	53.5	57
Volume of collagen [%]	30	24	27	33	36
Orientation α [°]	6.91	4.09	5.5	8.32	9.73
κ_{ip}	0.28	0.23	0.26	0.30	0.33
κ_{op}	0.493	0.475	0.484	**0.497**	**0.499**

References

[1] P Lu et al. “Extracellular matrix degradation and remodeling in development and disease”. In: *Cold Spring Harbor Perspectives in Biology* 3 (2011), a005058.

[2] Jay D. Humphrey, Eric R. Dufresne, and Martin A. Schwartz. "Mechanotransduction and extracellular matrix homeostasis". In: *Nature Reviews Molecular Cell Biology* 15.12 (2014), pp. 802–812. DOI: 10.1038/nrm3896. URL: https://doi.org/10.1038/nrm3896.

[3] HL. Kim. "Arterial stiffness and hypertension." In: *Clinical Hypertension* 1 (2023), 29(1):31. DOI: 0.1186/s40885-023-00258-1.

[4] Ernesto L. Schiffrin. "How Structure, Mechanics, and Function of the Vasculature Contribute to Blood Pressure Elevation in Hypertension". In: *Canadian Journal of Cardiology* 36.5 (2020), pp. 648–658. ISSN: 0828-282X. DOI: https://doi.org/10.1016/j.cjca.2020.02.003. URL: https://www.sciencedirect.com/science/article/pii/S0828282X20300751.

[5] Hope D. Intengan and Ernesto L. Schiffrin. "Structure and Mechanical Properties of Resistance Arteries in Hypertension". In: *Hypertension* 36.3 (2000), pp. 312–318. DOI: 10.1161/01.HYP.36.3.312. eprint: https://www.ahajournals.org/doi/pdf/10.1161/01.HYP.36.3.312. URL: https://www.ahajournals.org/doi/abs/10.1161/01.HYP.36.3.312.

[6] Manli Zhou et al. "Wall shear stress and its role in atherosclerosis". In: *Frontiers in Cardiovascular Medicine* 10 (2023). ISSN: 2297-055X. DOI: 10.3389/fcvm.2023.1083547. URL: https://www.frontiersin.org/journals/cardiovascular-medicine/articles/10.3389/fcvm.2023.1083547.

[7] A. Lusis. "Atherosclerosis". In: *Nature* 407 (2000), pp. 233–241. DOI: 10.1038/35025203.

[8] Nele Famaey and Jos Vander Sloten. "Soft tissue modelling for applications in virtual surgery and surgical robotics". In: *Computer Methods in Biomechanics and Biomedical Engineering* 11.4 (2008). Published online: 06 Jun 2008, pp. 351–366. DOI: 10.1080/10255840802020412. URL: https://doi.org/10.1080/10255840802020412.

[9] Martin A. Zulliger, Alexander Rachev, and Nikos Stergiopulos. "A constitutive formulation of arterial mechanics including vascular smooth muscle tone". In: *American Journal of Physiology-Heart and Circulatory Physiology* 287.3 (2004), H1335–H1343. DOI: 10.1152/ajpheart.00094.2004. URL: https://doi.org/10.1152/ajpheart.00094.2004.

[10] Ellen M. Arruda and Mary C. Boyce. "A three-dimensional constitutive model for the large stretch behavior of rubber elastic materials". In: *Journal of the Mechanics and Physics of Solids* 41.2 (1993), pp. 389–412. ISSN: 0022-5096. DOI: https://doi.org/10.1016/0022-5096(93)90013-6. URL: https://www.sciencedirect.com/science/article/pii/0022509693900136.

[11] T. C. Gasser, R. W. Ogden, and G. A. Holzapfel. "Hyperelastic modelling of arterial layers with distributed collagen fibre orientations". In: *Journal of the Royal Society, Interface* 3.6 (2006), pp. 15–35. DOI: 10.1098/rsif.2005.0073.

[12] M.G.D. Geers, V.G. Kouznetsova, and W.A.M. Brekelmans. "Multi-scale computational homogenization: Trends and challenges". In: *Journal of Computational and Applied Mathematics* 234.7 (2010). Fourth International Conference on Advanced COmputational Methods in ENgineering (ACOMEN 2008), pp. 2175–2182. ISSN: 0377-0427. DOI: https://doi.org/10.1016/j.cam.2009.08.077. URL: https://www.sciencedirect.com/science/article/pii/S0377042709005536.

[13] V. Kouznetsova, W. A. M. Brekelmans, and F. P. T. Baaijens. "An approach to micro–macro modeling of heterogeneous materials". In: *Computational Mechanics* 27 (2001), pp. 37–48. DOI: 10.1007/s004660000212. URL: https://doi.org/10.1007/s004660000212.

[14] Lauranne Maes et al. "Cell signaling and tissue remodeling in the pulmonary autograft after the Ross procedure: A computational study". In: *Journal of Biomechanics* 171 (June 2024), p. 112180. DOI: 10.1016/j.jbiomech.2024.112180. URL: https://doi.org/10.1016/j.jbiomech.2024.112180.

[15] Frédéric Feyel. "A multilevel finite element method (FE2) to describe the response of highly non-linear structures using generalized continua". In: *Computer Methods in Applied Mechanics and Engineering* 192.28 (2003). Multiscale Computational Mechanics for Materials and Structures, pp. 3233–3244. ISSN: 0045-7825. DOI: https://doi.org/10.1016/S0045-7825(03)00348-7. URL: https://www.sciencedirect.com/science/article/pii/S0045782503003487.

[16] Issam Doghri. *Mechanics of Deformable Solids*. Springer, 2000. Chap. 20.

[17] "Structural modeling reveals microstructure-strength relationship for human ascending thoracic aorta". In: *Journal of Biomechanics* 71 (2018), pp. 84–93. ISSN: 0021-9290. DOI: https://doi.org/10.1016/j.jbiomech.2018.01.037. URL: https://www.sciencedirect.com/science/article/pii/S0021929018300745.

[18] Ryan R. Mahutga and Victor H. Barocas. "Investigation of Pathophysiological Aspects of Aortic Growth, Remodeling, and Failure Using a Discrete-Fiber Microstructural Model". In: *Journal of Biomechanical Engineering* 142(11), 111007 (2020). DOI: https://doi.org/10.1115/1.4048031.

[19] D.C.D. Speirs, E.A. de Souza Neto, and D. Perić. "An approach to the mechanical constitutive modelling of arterial tissue based on homogenization and optimization". In: *Journal of Biomechanics* 41.12 (2008), pp. 2673–2680. ISSN: 0021-9290. DOI: https://doi.org/10.1016/j.jbiomech.2008.06.020. URL: https://www.sciencedirect.com/science/article/pii/S0021929008003023.

[20] Hozhabr Mozafari et al. In: *Nanotechnology Reviews* 8.1 (2019), pp. 539–547. DOI: doi:10.1515/ntrev-2019-0048. URL: https://doi.org/10.1515/ntrev-2019-0048.

[21] S. B. Shah et al. "Prefailure and failure mechanics of the porcine ascending thoracic aorta: experiments and a multiscale model". In: *Journal of biomechanical engineering* (2014), 136(2), 021028. DOI: https://doi.org/10.1115/1.4026443. URL: https://doi.org/10.1515/ntrev-2019-0048.

[22] Misael Dalbosco et al. “Multiscale numerical analyses of arterial tissue with embedded elements in the finite strain regime”. In: *Computer Methods in Applied Mechanics and Engineering* 381 (2021), p. 113844. ISSN: 0045-7825. DOI: https://doi.org/10.1016/j.cma.2021.113844. URL: https://www.sciencedirect.com/science/article/pii/S004578252100181X.

[23] Misael Dalbosco, Eduardo A. Fancello, and Gerhard A. Holzapfel. “Multiscale computational modeling of arterial micromechanics: A review”. In: *Computer Methods in Applied Mechanics and Engineering* 425 (2024), p. 116916. ISSN: 0045-7825. DOI: https://doi.org/10.1016/j.cma.2024.116916. URL: https://www.sciencedirect.com/science/article/pii/S0045782524001725.

[24] Michael R. Hill et al. “A theoretical and non-destructive experimental approach for direct inclusion of measured collagen orientation and recruitment into mechanical models of the artery wall”. In: *Journal of Biomechanics* 45.5 (2012). Special Issue on Cardiovascular Solid Mechanics, pp. 762–771. ISSN: 0021-9290. DOI: https://doi.org/10.1016/j.jbiomech.2011.11.016. URL: https://www.sciencedirect.com/science/article/pii/S0021929011006981.

[25] Lisa Leyssens et al. “Non-destructive 3D characterization of the blood vessel wall microstructure in different species and blood vessel types using contrast-enhanced microCT and comparison with synthetic vascular grafts”. In: *Acta Biomaterialia* 164 (2023), pp. 303–316. ISSN: 1742-7061. DOI: https://doi.org/10.1016/j.actbio.2023.04.013. URL: https://www.sciencedirect.com/science/article/pii/S1742706123002052.

[26] Selda Sherifova et al. “Failure properties and microstructure of healthy and aneurysmatic human thoracic aortas subjected to uniaxial extension with a focus on the media”. In: *Acta Biomaterialia* 99 (2019), pp. 443–456. ISSN: 1742-7061. DOI: https://doi.org/10.1016/j.actbio.2019.08.038. URL: https://www.sciencedirect.com/science/article/pii/S174270611930594X.

[27] O’Connell M. K. et al. “The three-dimensional micro- and nanostructure of the aortic medial lamellar unit measured using 3D confocal and electron microscopy imaging.” In: *Matrix biology : journal of the International Society for Matrix Biology* 27(3) (2008), pp. 171–181. DOI: https://doi.org/10.1016/j.matbio.2007.10.008.

[28] *Creative Commons — Attribution 4.0 International — CC BY 4.0*. https://creativecommons.org/licenses/by/4.0/. Accessed on 22 May 2025.

[29] Alessandro Giudici, Ian B. Wilkinson, and Ashraf W. Khir. “Review of the Techniques Used for Investigating the Role Elastin and Collagen Play in Arterial Wall Mechanics”. In: *IEEE Reviews in Biomedical Engineering* 14 (2021), pp. 256–269. DOI: 10.1109/RBME.2020.3005448.

[30] “Multiscale Mechanical Behavior of Large Arteries”. In: *Encyclopedia of Biomedical Engineering*. Ed. by Roger Narayan. Oxford: Elsevier, 2019, pp. 180–202. ISBN: 978-0-12-805144-3. DOI: https://doi.org/10.1016/B978-0-12-801238-3.99934-3. URL: https://www.sciencedirect.com/science/article/pii/B9780128012383999343.

[31] Chang M. He and Margot R. Roach. “The composition and mechanical properties of abdominal aortic aneurysms”. In: *Journal of Vascular Surgery* 20.1 (1988), pp. 6–13.

[32] Justyna A Niestrawska et al. “Differences in Collagen Fiber Diameter and Waviness between Healthy and Aneurysmal Abdominal Aortas”. In: *Microscopy and Microanalysis* 28.5 (Oct. 2022), pp. 1649–1663. ISSN: 1431-9276. DOI: 10.1017/S1431927622000629. eprint: https://academic.oup.com/mam/article-pdf/28/5/1649/48814186/mam1649.pdf. URL: https://doi.org/10.1017/S1431927622000629.

[33] H. Miyazaki and K. Hayashi. “Tensile Tests of Collagen Fibers Obtained from the Rabbit Patellar Tendon”. In: *Biomedical Microdevices* 2 (1999), pp. 151–157. DOI: 10.1023/A:1009953805658. URL: https://doi.org/10.1023/A:1009953805658.

[34] Zbyněk Tonar et al. “Segmental and age differences in the elastin network, collagen, and smooth muscle phenotype in the tunica media of the porcine aorta”. In: *Annals of Anatomy - Anatomischer Anzeiger* 201 (2015), pp. 79–90. ISSN: 0940-9602. DOI: https://doi.org/10.1016/j.aanat.2015.05.005. URL: https://www.sciencedirect.com/science/article/pii/S0940960215000837.

[35] Justyna A. Niestrawska et al. “Microstructure and mechanics of healthy and aneurysmatic abdominal aortas: experimental analysis and modelling”. In: *Journal of the Royal Society Interface* 13.124 (2016), p. 20160620. DOI: 10.1098/rsif.2016.0620. URL: http://doi.org/10.1098/rsif.2016.0620.

[36] Gerhard A. Holzapfel et al. “Modelling non-symmetric collagen fibre dispersion in arterial walls”. In: *Journal of the Royal Society Interface* 12.106 (2015), p. 20150188. DOI: 10.1098/rsif.2015.0188. URL: http://doi.org/10.1098/rsif.2015.0188.

[37] M. Amabili et al. “Microstructural and mechanical characterization of the layers of human descending thoracic aortas”. In: *Acta Biomaterialia* 134 (2021), pp. 401–421. DOI: 10.1016/j.actbio.2021.07.036. URL: https://doi.org/10.1016/j.actbio.2021.07.036.

[38] Bane Sullivan and Alexander Kaszynski. *PyVista: 3D plotting and mesh analysis through a streamlined interface for the Visualization Toolkit (VTK)*. May 2019. DOI: 10.21105/joss.01450. URL: https://github.com/pyvista/pyvista.

[39] John Gosline et al. “Elastic Proteins: Biological Roles and Mechanical Properties”. In: *Philosophical Transactions: Biological Sciences* 357.1418 (2002), pp. 121–132. ISSN: 09628436. URL: http://www.jstor.org/stable/3066845 (visited on 11/21/2024).

[40] Héctor Sanz-Fraile and Jorge Otero. "Mechanical Properties of the Extracellular Matrix". In: *Handbook of the Extracellular Matrix: Biologically-Derived Materials*. Ed. by F. Raquel Maia, J. Miguel Oliveira, and Rui L. Reis. Cham: Springer International Publishing, 2024, pp. 73–88. ISBN: 978-3-031-56363-8. DOI: 10.1007/978-3-031-56363-8_5. URL: https://doi.org/10.1007/978-3-031-56363-8_5.

[41] S. Halvorsen, R. Wang, and Y. Zhang. "Contribution of Elastic and Collagen Fibers to the Mechanical Behavior of Bovine Nuchal Ligament". In: *Annals of Biomedical Engineering* 51.10 (2023), pp. 2204–2215. DOI: 10.1007/s10439-023-03254-6. URL: https://doi.org/10.1007/s10439-023-03254-6.

[42] M. Zhou, P. J. González, L. Van Haasterecht, et al. "Uniaxial mechanical stretch properties correlated with three-dimensional microstructure of human dermal skin". In: *Biomechanics and Modeling in Mechanobiology* 23 (2024), pp. 911–925. DOI: 10.1007/s10237-023-01813-3. URL: https://doi.org/10.1007/s10237-023-01813-3.

[43] Y. Zhu et al. "Temporal analysis of vascular smooth muscle cell elasticity and adhesion reveals oscillation waveforms that differ with aging". In: *Aging cell* 11.5 (2012), pp. 741–750. DOI: https://doi.org/10.1111/j.1474-9726.2012.00840.x.

[44] R. Chen and D. Dean. "Mechanical properties of stem cells from different sources during vascular smooth muscle cell differentiation". In: *Molecular & Cellular Biomechanics: MCB* 14.3 (2017), pp. 153–169. DOI: https://doi.org/10.3970/mcb.2017.014.153. URL: https://doi.org/10.3970/mcb.2017.014.153.

[45] Hannah Weisbecker, Michael J. Unterberger, and Gerhard A. Holzapfel. "Constitutive modelling of arteries considering fibre recruitment and three-dimensional fibre distribution". In: *Journal of The Royal Society Interface* 12.105 (2015), p. 20150111. DOI: 10.1098/rsif.2015.0111. eprint: https://royalsocietypublishing.org/doi/pdf/10.1098/rsif.2015.0111. URL: https://royalsocietypublishing.org/doi/abs/10.1098/rsif.2015.0111.

[46] A. R. Lawrence and K. J. Gooch. "Transmural pressure and axial loading interactively regulate arterial remodeling ex vivo". In: *American Journal of Physiology. Heart and Circulatory Physiology* 297.1 (2009), H475–H484. DOI: 10.1152/ajpheart.00972.2008. URL: https://doi.org/10.1152/ajpheart.00972.2008.

[47] S. Bose et al. "Exploring the Mechanical Properties and Performance of Type-I Collagen at Various Length Scales: A Progress Report". In: *Materials (Basel, Switzerland)* 15.8 (2022), p. 2753. DOI: 10.3390/ma15082753. URL: https://doi.org/10.3390/ma15082753.

[48] K. E. Aifantis, S. Shrivastava, and G. M. Odegard. "Transverse mechanical properties of collagen fibers from nanoindentation". In: *Journal of Materials Science: Materials in Medicine* 22 (2011), pp. 1375–1381. DOI: 10.1007/s10856-011-4320-9. URL: https://doi.org/10.1007/s10856-011-4320-9.

[49] Pavel Dutov et al. "Measurement of Elastic Modulus of Collagen Type I Single Fiber". In: *PLOS ONE* 11.1 (2016), e0145711. DOI: 10.1371/journal.pone.0145711. URL: https://doi.org/10.1371/journal.pone.0145711.

[50] A. Avanzini, D. Battini, and L. Giorleo. "Finite element modelling of 3D printed continuous carbon fiber composites: Embedded elements technique and experimental validation". In: *Composite Structures* 292 (2022), p. 115631. ISSN: 0263-8223. DOI: https://doi.org/10.1016/j.compstruct.2022.115631. URL: https://www.sciencedirect.com/science/article/pii/S0263822322004159.

[51] Vítor M.C.F. Cunha, Joaquim A.O. Barros, and José M. Sena-Cruz. "A finite element model with discrete embedded elements for fibre reinforced composites". In: *Computers Structures* 94-95 (2012), pp. 22–33. ISSN: 0045-7949. DOI: https://doi.org/10.1016/j.compstruc.2011.12.005. URL: https://www.sciencedirect.com/science/article/pii/S0045794911003038.

[52] Seung Yang et al. "Finite Element Analysis of RC Beams by the Discrete Model and CBIS Model Using LS-DYNA". In: *Advances in Civil Engineering* 2021 (Feb. 2021), pp. 1–9. DOI: 10.1155/2021/8857491.

[53] Dassault Systèmes - Simulia. *Abaqus 2009 Documentation: Abaqus/Constraints/Embedded Elements*. https://classes.engineering.wustl.edu/2009/spring/mase5513/abaqus/docs/v6.6/books/usb/default.htm?startat=pt08ch28s04aus111.html. Accessed: 2025-01-07. 2009.

[54] Laurence Brassart et al. "An extended Mori–Tanaka homogenization scheme for finite strain modeling of debonding in particle-reinforced elastomers". In: *Computational Materials Science - COMPUT MATER SCI* 45 (May 2009), pp. 611–616. DOI: 10.1016/j.commatsci.2008.06.021.

[55] Olivier Pierard. "Micromechanics of Inclusion-Reinforced Composites in Elasto-Plasticity and Elasto-Viscoplasticity: Modeling and Computation". (Available online). PhD thesis. Université catholique de Louvain, 2007.

[56] Ke Lu and Frans P. van der Meer. "A Computational Homogenization Framework with Enhanced Localization Criterion for Macroscopic Cohesive Failure in Heterogeneous Materials". In: *Journal of Theoretical, Computational and Applied Mechanics* 2 (2022), pp. 1–28. DOI: 10.46298/jtcam.7707.

[57] Heleen Fehervary et al. "Planar biaxial testing of soft biological tissue using rakes: A critical analysis of protocol and fitting process". In: *Journal of the Mechanical Behavior of Biomedical Materials* 61 (2016), pp. 135–151. ISSN: 1751-6161. DOI: https://doi.org/10.1016/j.jmbbm.2016.01.011. URL: https://www.sciencedirect.com/science/article/pii/S175161611600014X.

[58] Heleen Fehervary et al. "How important is sample alignment in planar biaxial testing of anisotropic soft biological tissues? A finite element study". In: *Journal of the Mechanical Behavior of Biomedical Materials* 88 (2018), pp. 201–216. ISSN: 1751-6161. DOI: https://doi.org/10.1016/j.jmbbm.2018.06.024. URL: https://www.sciencedirect.com/science/article/pii/S1751616118303710.

[59] Klaas Vander Linden et al. “An improved parameter fitting approach of a planar biaxial test including the experimental pre-stretch”. In: *Journal of the Mechanical Behavior of Biomedical Materials* 134 (2022), p. 105389. ISSN: 1751-6161. DOI: https://doi.org/10.1016/j.jmbbm.2022.105389. URL: https://www.sciencedirect.com/science/article/pii/S1751616122002971.

[60] Nele Famaey et al. *C4Bio: Community Challenge Towards Consensus on Characterization of Biological Tissue*. Abstract/Presentation/Poster. Presented at the Virtual Physiological Human (VPH) conference , 2022. Sept. 2022.

[61] Monika Jain and Anil K. Chauhan. “Role of Integrins in Modulating Smooth Muscle Cell Plasticity and Vascular Remodeling: From Expression to Therapeutic Implications”. In: *Cells* 11.4 (2022), p. 646. DOI: 10.3390/cells11040646. URL: https://doi.org/10.3390/cells11040646.

[62] Agne Frismantiene et al. “Cadherins in vascular smooth muscle cell (patho)biology: Quid nos scimus?” In: *Cellular Signalling* 45 (2018), pp. 23–42. DOI: 10.1016/j.cellsig.2018.01.023.

[63] X. Chen et al. “Glycosaminoglycans modulate long-range mechanical communication between cells in collagen networks”. In: *Proceedings of the National Academy of Sciences of the United States of America* 119.15 (2022), e2116718119. DOI: 10.1073/pnas.2116718119. URL: https://doi.org/10.1073/pnas.2116718119.

[64] Antonio Lepedda et al. “Glycosaminoglycans: From Vascular Physiology to Tissue Engineering Applications”. In: *Frontiers in Chemistry* 9 (2021). DOI: 10.3389/fchem.2021.680836. URL: https://doi.org/10.3389/fchem.2021.680836.

[65] G. A. Ateshian et al. “Finite-element implementation of mechanochemical phenomena in neutral deformable porous media under finite deformation”. In: *Journal of Biomechanical Engineering* 133.8 (2011), p. 081005. DOI: 10.1115/1.4004810.

[66] Sara Roccabianca, Chiara Bellini, and J. D. Humphrey. “Computational modelling suggests good, bad and ugly roles of glycosaminoglycans in arterial wall mechanics and mechanobiology”. In: *Journal of the Royal Society Interface* 11.97 (2014). DOI: 10.1098/rsif.2014.0397. URL: https://doi.org/10.1098/rsif.2014.0397.

[67] Gerhard A. Holzapfel. “Determination of material models for arterial walls from uniaxial extension tests and histological structure”. In: *Journal of Theoretical Biology* 238.2 (2006), pp. 290–302. DOI: 10.1016/j.jtbi.2005.05.006. URL: https://doi.org/10.1016/j.jtbi.2005.05.006.

[68] Pjotr L. J. Hilhorst et al. “Efficient sensitivity analysis for biomechanical models with correlated inputs”. In: *International Journal for Numerical Methods in Biomedical Engineering* 1.1 (2023). First published: 20 December 2023, pp. 1–15. DOI: 10.1002/cnm.3797. URL: https://doi.org/10.1002/cnm.3797.

[69] A. Menichetti et al. “A Machine Learning Approach to Investigate the Uncertainty of Tissue-Level Injury Metrics for Cerebral Contusion”. In: *Frontiers in Bioengineering and Biotechnology* 9 (2021). DOI: 10.3389/fbioe.2021.714128. URL: https://doi.org/10.3389/fbioe.2021.714128.

[70] Lauren Irons and Jay D. Humphrey. “Cell signaling model for arterial mechanobiology”. In: *PLoS Computational Biology* 16.8 (2020), e1008161. DOI: 10.1371/journal.pcbi.1008161. URL: https://doi.org/10.1371/journal.pcbi.1008161.

[71] S. M. Flanary et al. “A computational bridge between traction force microscopy and tissue contraction”. In: *Journal of Applied Physics* 134.7 (2023), p. 074901. DOI: 10.1063/5.0157507. URL: https://doi.org/10.1063/5.0157507.

[72] S. M. Flanary and V. H. Barocas. “A structural bio-chemo-mechanical model for vascular smooth muscle cell traction force microscopy”. In: *Biomechanics and Modeling in Mechanobiology* (2023). [HTML]. DOI: 10.1007/s10237-023-01658-6. URL: https://link.springer.com/article/10.1007/s10237-023-01658-6.

[73] Denisa Martonová et al. “Automated model discovery for human cardiac tissue: Discovering the best model and parameters”. In: *Computer Methods in Applied Mechanics and Engineering* 418 (2024), p. 117078. DOI: 10.1016/j.cma.2024.117078.

[74] T. Vervenne et al. “Constitutive neural networks for main pulmonary arteries: discovering the undiscovered”. In: *Biomechanics and Modeling in Mechanobiology* (2025). DOI: 10.1007/s10237-025-01930-1. URL: https://doi.org/10.1007/s10237-025-01930-1.

[75] Hagen Holthusen et al. “Polyconvex inelastic constitutive artificial neural networks”. In: *Proceedings in Applied Mathematics and Mechanics (PAMM)* (2024). First published: 18 September 2024. DOI: 10.1002/pamm.202400032. URL: https://doi.org/10.1002/pamm.202400032.

[76] Mohammadhossein Ebrahimi et al. “Elastic, Viscoelastic and Fibril-Reinforced Poroelastic Material Properties of Healthy and Osteoarthritic Human Tibial Cartilage”. In: *Annals of Biomedical Engineering* 47.4 (2019), pp. 953–966. DOI: 10.1007/s10439-019-02213-4.

[77] Seyed Ali Elahi et al. “Guide to mechanical characterization of articular cartilage and hydrogel constructs based on a systematic in silico parameter sensitivity analysis”. In: *Journal of the Mechanical Behavior of Biomedical Materials* 124 (2021), p. 104795. ISSN: 1751-6161. DOI: 10.1016/j.jmbbm.2021.104795. URL: https://doi.org/10.1016/j.jmbbm.2021.104795.

[78] Arne Maes et al. “Cryogenic contrast-enhanced microCT enables nondestructive 3D quantitative histopathology of soft biological tissues”. In: *Nature Communications* 13.1 (2022), pp. 1–14.